Miocene andalusite leucogranite in central-east Himalaya (Everest–Masang Kang area): Low-pressure melting during heating

05/04/2012

MIOCENE ANDALUSITE LEUCOGRANITE IN CENTRAL-EAST HIMALAYA (EVEREST-MASANG KANG AREA): LOW-PRESSURE MELTING DURING HEATING

Dario VISONA' [a], ***Rodolfo CAROSI*** [b], ***Chiara MONTOMOLI*** [c], ***Massimo TIEPOLO*** [d] ***and Luca PERUZZO*** [e]

a Dipartimento di Geoscienze, University of Padova, Padova, Italy. dario.visona@unipd.it
b Dipartimento di Scienze della Terra, University of Torino, Torino, Italy. carosi@unito.it
c Dipartimento di Scienze della Terra, University of Pisa, Pisa, Italy. montomoli@dst.unipi.it
d C.N.R.-Istituto di Geoscienze e Georisorse. UOS Pavia, via Ferrata 1 27100 Pavia, Italy. tiepolo@crystal.unipv.it
e C.N.R.-Istituto di Geoscienze e Georisorse – Sez.di Padova c/o Dip. di Geoscienze - University of Padova, Padova, Italy. peruzzo@igg.cnr.it

Corresponding author: Dario Visonà, Dipartimento di Geoscienze, University of Padova, via Gradenigo 6, I-35131 Padova, Italy. dario.visona@unipd.it tel. +390498279147

Abstract

The studied Miocene andalusite-bearing leucogranites intrude the upper part of the High Himalayan Crystallines (HHC) and the north Himalayan domes and outcrop in an area stretching from Mt. Everest to the Kula Khangri massif (Bhutan) towards the east.

The leucogranites constitute both dykes as wel as sills and parts of larger andalusite-free leucogranite plutons (e.g., Makalu). They represent mainly of two-mica (muscovite+biotite ±tourmaline±cordierite±andalusite±sillimanite±dumortierite) leucogranite, and tourmaline (muscovite+tourmaline±biotite±andalusite±sillimanite±garnet±kyanite±spinel±corundum) leucogranites. Microstructures reveal several generations of andalusite (from residual/peritectic early magmatic to cotectic late magmatic), even in the same sample. The occurrence of residual and/or peritectic andalusite, together with inclusions of sillimanite+biotite in cordierite, indicates that melts formed by dehydration melting of biotite at T = 660-700 °C during prograde heating at low-pressure conditions (P< about 400 MPa).

According to current models, leucogranites are produced by dehydration melting of muscovite and/or biotite during exhumation of the HHC. In this case, micas are consumed in the sillimanite stability field. As a consequence, these models cannot explain the occurrence of residual and/or peritectic magmatic andalusite. Conditions for anatexis in the andalusite field may have been achieved by heat transfer within the exhuming (extruding) HHC, from structurally lower and hotter rocks towards upper and colder fertile lithologies.

***Keywords*:** Andalusite leucogranite; Miocene; High Himalayan Crystallines; U-Pb zircon geochronology; Petrology.

1. Introduction

Andalusite is a mineral found in peraluminous felsic igneous rocks, the petrological importance of which is mainly associated with its relatively limited chemical and, particularly, physical ranges of stability in melts. The composition of the source rock, degree of water saturation and alumina content of the melt are among the most important chemical factors controlling the stability of andalusite in granitic rocks (Acosta-Vigil et al., 2002, 2003; Clarke et al., 2005; Clarke et al., 2009). The essential condition for the occurrence of magmatic andalusite in granitic rocks is also that magma should have been generated or crystallised at a P< about 400 MPa (e.g. Pattison, 1992). Of course andalusite may also be found in granitic rocks as a xenocrystic mineral inherited from the local country rocks but, in this case, it has no meaning for granite petrology (e.g., Clarke, 2007).

Following many previous authors, the Himalayan leucogranites in this and other areas originated from partial melting of the crystalline basement (High Himalayan Crystallines: HHC) in response to rapid exhumation during the incongruent melting of muscovite at intermediate pressure values (P~600-400 MPa, T~700 °C), followed by crystallisation at P~400 MPa (e.g. Searle et al., 2010; Streule et al., 2010; and references therein). In this framework, formation of andalusite should be limited to the final stages of crystallisation, as suggested for the Miocene leucogranite of Central Bhutan (Kellett et al., 2009). However, most of the Himalayan andalusite-bearing leucogranite described in the literature (e.g., Visonà and Lombardo, 2002; Castelli and Lombardo 1988, Pognante and Benna 1993) shows textures indicating that andalusite is an early crystallisation phase. This evidence strongly suggests that the Himalayan andalusite-bearing leucogranite formed at pressures lower than those predicted by decompressional melting models (Searle et al., 2010).

The aim of this paper is to present and discuss the features of the Himalayan Miocene andalusite-bearing leucogranite in a larger area and in greater detail than in the previous work by Visonà and Lombardo (2002), and to explore the possibility that its formation is related to low-pressure regional heating instead of decompressional melting.The petrographic characteristics of andalusite leucogranite from the literature of the Himalayas are reviewed, and details of the petrography, mineral chemistry, minimal geochemistry and geochronology of new samples from an area east of Mt. Everest are provided. These petrographic observations are compared with those reviewed by Clarke et al. (2005) on the origin of andalusite in granites.

2. Geological framework

2.1 The Himalaya Orogen and the Cenozoic granite belts

The collision of the Indian continent with the Asia plate in the Cenozoic gave rise to the well-known Himalayan architecture, which is composed of five lithotectonic domains forming parallel belts, separated by four main tectonic lines (Gansser, 1964; Le Fort, 1975). From south to north, the Main Boundary Thrust separates Sub-Himalaya from Lower Himalaya; the Main Central Thrust separates Lower Himalaya from Higher Himalaya and, further north, the South Tibetan Detachment separates Higher Himalaya from Tibetan Himalaya. Lastly, the Indus-Tsangpo suture defines the Tibetan Plateau to the north. The Trans-Himalayan Batholith, an I-type plutonic complex originated by subduction of the oceanic crust of the Tethys Sea between 140 and 40 Ma, is located at the southern margin of the Tibetan Plateau (Fig 1).

Higher Himalaya is carved out of a huge thrust sheet (the Higher Himalayan Crystallines, HHC) composed of metamorphic rocks in the upper amphibolite to granulite facies and migmatites characterised by a metamorphism of Tertiary age. The HHC contains two magmatic belts consisting of S-type granite of Miocene age, the High Himalaya Granite (HHG) and North Himalayan Granite (NHG). These two belts extend from Zanskar as far as Central Bhutan and are mainly concentrated in the Central and Eastern Himalayas. The HHG forms a chain of small plutons or more commonly a network of dykes in the upper HHC (north of the High Himalayan Thrust; HHT in Fig. 1), near the South Tibetan Detachment which separates the High Himalayan Crystallines from Tibetan Himalaya. The NHG comprises a series of independent plutonic bodies intruding the gneissic dome which are considered as windows of the HHC below the Tibetan Himalaya (e.g., Larson et al., 2010; Lee et al., 2004), the sedimentary series of the pre-collision continental shelf of the India plate.

The HHG and NHG are generally classified as leucogranites (Debon and Le Fort, 1983) although many of these rocks have modal contents of mafic minerals exceeding 5% vol. (e.g. Visonà and Lombardo, 2002). They are peraluminous (ASI= 1.08-1.34: Debon et al., 1986; Castelli and Lombardo, 1988; Visonà and Lombardo, 2002; data reported in Acosta-Vigil et al., 2003; Zhang et al., 2004; this paper) and, according to the modal contents of tourmaline and biotite, two main types are identified (Guillot and Le Fort 1995; Dèzes, 1999; Visonà and Lombardo, 2002): i) a *two-mica* type (2mg, with tourmaline <2.6% and biotite > 1.5%), also including minor biotite granite containing scarce magmatic muscovite; ii) a less abundant *tourmaline leucogranite* (Tg, with tourmaline > 2.2% and biotite up to 1.5%). Both types may contain not only toumaline but also other peraluminous minerals such as cordierite or, less commonly, garnet, sillimanite, andalusite, corundum, beryl, and rare xenocrystic kyanite. Both types intruded the same high structural level of

the HHC, and cross-cutting relationships in plutons and dyke swarms indicate in most cases that 2mg intruded first and the Tg are the latest (Visonà and Lombardo, 2002, and references therein).

2.2 Andalusite-bearing leucogranite

Andalusite has been described in leucogranites of both granitic belts (HHG and NHG) since the early petrographic studies (Bordet, 1961; Palivcova et al., 1982; Debon et al., 1986; Pognante and Benna, 1993); it was only reported, however, in a limited number of locations. The most recent studies (Visonà and Lombardo, 2002; Rolfo et al., 2006; Kellet et al., 2009; Mosca et al., 2010) extend the areas with andalusite leucogranites to a larger sector of the central-eastern part of the Himalayan range (Figs. 1 and 2). From west to east, these occurrences are: *Gneissic domes* in the Tibetan Himalaya; *Makalu area; Khama-Phung Chu (Kharta)-Rongbuk area; Kangchenjunga and NE Sikkim areas; Central Bhutan.*

The gneissic domes in the Tibetan Himalaya are exposed by the North Himalayan antiform in southern Tibet, NE of Mount Everest. The Lagoi Kangri and Mabja-Kuday domes are intruded by two-mica granite (with biotite > muscovite) containing sillimanite, garnet, andalusite and xenocrystic kyanite (Debon et al., 1986; Zhang et al., 2004, Lee et al., 2006).

In the *Makalu area*, andalusite occurs in tourmaline granite and two-mica granite collected in the upper part of the Barun glacier basin, at the bottom of the West Wall of Makalu (Bordet, 1961; Pognante and Benna, 1993; Visonà and Lombardo, 2002). Andalusite two-mica granite was already described and sampled along the West Wall by Palivcova et al. (1982). The Makalu pluton is the result of the intrusion of two magmatic pulses, the first at 24-21 Ma and 15.6±0.2 Ma, respectively (Schärer et al., 1984; Streule et al., 2010). According to Streule et al. (2010), however, both pulses are composed of leucogranite with tourmaline and cordierite, and andalusite was not reported by these authors.

In the *Kama-Phung Chu (Kharta)-Rongbuk area* (NNE of Makalu), the HHC is intruded by numerous dykes or small subcorcordant bodies of leucogranite, often with andalusite ± cordierite and/or sillimanite (Visonà and Lombardo, 2002; Cottle et al., 2009a). In most cases, these are examples of medium- to fine-grained two-mica granite, commonly containing pods or orbicules of tourmaline+quartz; tourmaline granite is less abundant and usually foliated.

In the *Kangchenjunga area*, the occurrence of andalusite leucogranite has been reported both on the Nepalese (Mosca et al., 2010) and Indian (Sikkim) flanks (Zemu valley; Rolfo et al., 2006). In both cases, dykes are composed of medium- to fine-grained two-mica granite with pods of tourmaline + quartz.

In *Central Bhutan* (SW of Kula Kangri), andalusite-bearing leucogranites have been found in sills and networks of dykes (Castelli and Lombardo, 1988; Kellet et al., 2009), commonly containing also cordierite and sillimanite.

3. Petrography

In the Everest-Sikkim area (Fig. 1), andalusite is mainly found in two-mica granite pertaining to both the NHG and HHG belts, and only to a lesser extent in tourmaline granite. Andalusite has been also found, although only once (Zemu glacier valley), as a vein mineral within the two-mica granite. The new data we present on the andalusite leucogranites of the HHG belts outcropping in the area of Fig. 2, include the scarce petrographic and geochemical data available in the literature regarding the gneissic domes of Tibetan Himalaya and Central Bhutan (Tab. 6).

Regarding bulk rock major element compositions, andalusite-bearing leucogranites are indistinguishable from andalusite-free leucogranites and both are classified as moderately to strongly peraluminous granites. The andalusite leucogranites have an ASI between 1.11 and 1.29 (ASI = molecular ratio of $Al_2O_3/(CaO+Na_2O+K_2O)$; Zen 1986), are characterised by high SiO_2 and low $FeOt+MgO+TiO_2$ concentrations (Tab. 6), and plot close to the minimum or eutectic melt compositions in the pseudo-ternary Qtz-Or-Ab aplogranite space (at variable aH_2O conditions and pressures between 200 and 500 MPa; Visonà and Lombardo, 2002). With the aim of ascertaining the origin of the andalusite in the Himalayan leucogranites, the following petrographic description refers to the textural and chemical criteria recently discussed by Clarke et al. (2005): *size* (compatibility or incompatibility with grain sizes of igneous minerals in the same rock), *shape* (ranging from euhedral to anhedral),and state of aggregation of andalusite (single grains, type S, or clusters of grains, type C), and its *association with muscovite* (presence or absence of monocrystalline or polycrystalline muscovite rims), and the *compositions* of coexisting minerals. Following these criteria, the three main genetic types of andalusite in felsic igneous rocks have been found in the Himalayan leucogranite: Type 1 Metamorphic (prograde and retrograde metamorphic, xenocrystic and residual), Type 2 Magmatic, and Type 3 metasomatic (Clarke et al., 2005).

3.1. Andalusite in leucogranites. *Andalusite tourmaline granite* occurs as medium- to coarse-grained, mostly foliated rocks, characterised by abundant muscovite and tourmaline and scarce biotite. Apatite is abundant and appears as euhedral to anhedral grains; zircon and monazite are less abundant accessories. Thin fibrous sillimanite occurs as inclusions in muscovite present in millimetric shear zones of the foliated rock. Hercynite and euhedral garnet (Spessartine: Alm27Sps70Andr3) are occasionally present (Visonà and Lombardo, 2002). Sample V916 contains xenocrystic corundum (up to 3 mm in length) included in feldspar. Andalusite is commonly pink in

colour and its crystal size is slightly larger than that of the other rock-forming minerals (up to 8 mm). Andalusite appears in single grains (S textural type, see below), fractured and deeply corroded by muscovite monocrystalline overgrowths. In some cases, euhedral andalusite is found included in tourmaline.

Andalusite two-mica granite are typically fine- to medium-grained rocks, in some cases foliated, and are located mainly in the HHG. Peraluminous minerals such as andalusite, cordierite, sillimanite and reddish-purple dumortierite are common and relatively abundant. The dumortierite grains contain plagioclase and rounded quartz, and are variably transformed into muscovite. Rare Al-spinel and relics of corundum ± prismatic sillimanite (V731, V953) occur in plagioclase. Brown fibrous sillimanite usually fills mineral junctions in the matrix (Fig. 3a, e, f), and forms trails surrounding andalusite (when not enclosed in plagioclase; Fig. 3m). Acicular sillimanite preferentially grows on biotite borders or as fans of diverging needles in biotite and muscovite (Fig. 3n). Cordierite is found as euhedral crystals, in places replaced by chlorite+muscovite, and in some samples wrapped by tourmaline. Some euhedral cordierite host relics of an older association of biotite+prismatic sillimanite, a texture interpreted as indicating magmatic-peritectic growth of cordierite during biotite melting reactions (Visonà and Lombardo, 2002). Andalusite occurs in quantities up to 5% modal (Makalu, Palivcova et al., 1982), in pink crystals with colourless rims. It can be either similar in size (size-compatible) or much smaller (size-incompatible) than the essential minerals, and more rarely much larger (size-incompatible) than the matrix minerals (granite from the Zemu glacier valley, VS10). Together with the other mineralogical components, the andalusite gives origin to a wide range of microstructures referred to the various textural classes of Clarke et al. (2005), summarised below.

3.2. Andalusite textural types

Type S: this is represented by euhedral to subhedral single grains in the matrix, and may also be found included in plagioclase cores. All types of microstructures, from those without muscovitic rims up to crystals almost completely replaced by large muscovite flakes, are observed (Fig 3g), in some cases in textural equilibrium with biotite (Fig. 3d). Subhedral to euhedral andalusite may be replaced by fibrolitic sillimanite or acicular (topotactic) sillimanite (Fig. 3l). Single subhedral to anhedral crystals lacking a muscovite mantle are found in the cores of zoned plagioclase (Fig. 3c). Relicts of corundum and prismatic sillimanite are found in the plagioclase of sample V731, together with anhedral andalusite.

Type C: is formed of two different types of clusters of randomly oriented grains, smaller than the magmatic minerals (size-incompatible). **a)** Optically discontinuous aggregates of subhedral to rounded crystals of variable size (0,05-0.25 mm), tightly packed and sometimes with brown

fibrolite borders (V928), interstitial or included in biotite, feldspar and quartz; remarkably, when these clusters are hosted in biotite or plagioclase, the brown fibrolite border is missing (Fig. 3e, f and m). **b)** Aggregates of euhedral crystals (0.15-0.3 mm), interstitial between the larger magmatic crystals, and in places with a muscovite monocrystalline mantle (Fig. 3i). The two-mica leucogranite from the Zemu glacier valley (VS10) is peculiar in that it consists of a medium-grained (5 mm) granular rock with random quartz-K-feldspar graphic intergrowths containing skeletal muscovite, suggesting rapid and cotectic crystallisation. Here andalusite is found in crystals up to 16 mm long, subparallel and grouped to form "veins" of poikilitic and in places skeletal grains. The most common mineral inclusions in these poikilitic/skeletal crytals are laths of plagioclase, rounded quartz and, more rarely, anhedral K-feldspar and subhedral biotite. Andalusite is typically replaced by large monocrystalline muscovite, which may penetrate deeply along cracks, isolating rounded fragments.

4. Mineral chemistry

Mineral analyses were carried out with WDS CAMECA SX 50 electron microprobes operating at 20 kV and 10 nA, with integration time of 10 s for major elements and 10 s for minor elements; natural and synthetic pure oxides were used as standards for calibration. A PAP program was used to convert counts into weight percents of oxides. Results are considered accurate to within ±2% relative for major elements and ±5% for minor elements.

Muscovite flakes growing on andalusite, single euhedral crystals in the matrix isolated from biotite, and muscovite with euhedral contacts against biotite, were all analysed. Representative analyses are listed in Tab. 1**.** Only a few of the muscovite grains have TiO_2 concentrations > 1 wt%, suggesting a magmatic origin according to Miller et al. (1981). In undeformed granite, although the Na/(Na+K) ratio is > 0.06 (magmatic according to Monier et al., 1984, and Clarke et al., 2005), TiO_2 contents of muscovite in single flakes far from biotite or growing on andalusite, were commonly lower than those of muscovite in textural equilibrium with biotite. In the three samples of foliated granite analysed (Tab. 2b), one two-mica granite (V953) and two tourmaline granites (V218 and V927), the muscovite overgrowths on andalusite have TiO_2 <0.05% and Na/(Na+K)<0.06.

Biotite crystals have high alumina contents over a very restricted interval (Al^{IV}=2.68±0.07, n=82*;* Tab.1; Fig. 4a), suggesting that an Al-rich phase such as andalusite buffered the activity of Al_2O_3 in the system during crystallisation. The composition of the texturally co-existing pairs of muscovite-biotite are shown in Fig. 4b; the similar slope between all the tie-lines indicates that these two minerals reached chemical equilibrium. The D_{Ti}^{Bt-Ms} ranges between 1.30-22.07;

239 excluding all values exceeding 8 (as recommended by Clarke et al., 2005), the mean value is
240 4.51±2.3 (n=22). For micas with the above microstructures and compositions, this equilibrium was
241 probably established in magmatic rather than subsolidus-hydrothermal conditions (Brigatti et al.,
242 2000, Clarke et al., 2005).

243 Cordierite has only been found in two-mica granites. Euhedral crystals comparable in size
244 with the quartzo-feldspathic matrix (but showing contrasting microstructures) were analyzed
245 (analyzed crystals come from samples V23, Makalu; V472, Langma la; V93, Kharta). The
246 *Fe/(Fe+Mg)* ratio shows small variations (0.55-0.58) in samples V23 and V93, but a large variation
247 in V472 (0.43-0.64; Tab 4). The cordierite in sample V23 shows well-defined chemical zoning,
248 with the rim impoverished in MgO and Na_2O. In general the high Na_2O contents (up to 1.52 wt %)
249 and abundance of channel cations (Ca, Na and K; Tab 4) found in all crystals are very similar to
250 those of cordierite considered to crystallise from a felsic magma (e.g., Pereira and Bea, 1994 and
251 references therein; Alasino et al., 2010).

252

253 **5. U-Pb zircon geochronology**

254 *5.1 Methods*

255 In-situ U-Pb geochronology was carried out by excimer laser ablation-ICPMS at the C.N.R.-
256 IGG-U.O.S. of Pavia. Zircons were separated from granite sample V275 by conventional methods
257 (crushing, heavy liquids, hand-picking). Zircons as free as possible from fractures and inclusions
258 were mounted in epoxy resin, polished and characterised for internal structure by
259 cathodoluminescence (CL). The laser ablation instrument couples an ArF excimer laser microprobe
260 at 193 nm (Geolas200Q-Microlas) with a sector field high-resolution ICPMS Element I from
261 Thermo Finnigan. The analytical method is described by Tiepolo (2003). Instrumental and laser-
262 induced U/Pb fractionation values were corrected with the Plesovice zircon as external standard
263 (Slama et al., 2008). The same integration intervals and spot sizes were used on both external
264 standard and unknowns. The reference zircon 02123 (295 Ma; Ketchum et al., 2001) was analysed
265 together with unknowns for quality control (Tab 4). Spot size was set at 20 microns and laser
266 fluency at 12J/cm^2. Data reduction was carried out with the Glitter software package (van
267 Achterbergh et al., 2001) and reproducibility of standards was propagated to all determinations in
268 quadrature. Concordia ages were determined and concordia plots were constructed with Isoplot/EX
269 3.0 software (Ludwig, 2000). All errors are given at 2σ level.

270 *5.2 Results*

271 Zircon has prismatic habit and dimensions of 50 to 150 microns. CL images reveal a
272 complex internal structure characterised by inner and external domains with different properties

(Fig. 5). The inner cores are bright and showed oscillatory or convolute zoning. The boundary between the inner and external domains is lobate and cuts the internal structures, indicating that partial resorption occurred. The inner cores are thus inherited zircons. The outer domains have low CL emissions and show relatively well-developed oscillatory zoning, typical of zircon growth in magmatic conditions.

Thirty-six U-Pb geochronologic determinations were carried out on both internal and external domains, and most of the results yielded concordant U-Pb ages. Seven analyses carried out on the external domains with low CL emission yielded concordant or slightly discordant Miocene ages (discordance 1.7% to 4.6%). The mean concordia age was 15.9 ± 0.4 Ma (MSWD= 2.9; Fig. 5). The ages of inherited cores ranged from 375 Ma to 1613 Ma, with major intermediate clusters at 440 Ma and 780 Ma.

6. DISCUSSION

6.1 Origin of andalusite

6.1.1 Major element composition of leucogranites.

The geochemical data of Visonà and Lombardo (2002) show that the leucogranites examined here (Tab. 6) have normative compositions near that of a low-pressure *minimum melt* (P=300-350 MPa) in the wet haplogranite system . According to this and to the experimental data of Acosta-Vigil et al. (2003, 2006), the andalusite-bearing leucogranites are interpreted as low-pressure and relatively low-temperature melt rich in H_2O. For instance, the mean ASI value of 1.17 matches the ASI of melts rich in H_2O in equilibrium with andalusite at the temperatures suggested by the normative compositions and Zrn and Mnz saturation thermometry (647-798 °C, Tab. 6). In addition, the occurrence of peritectic cordierite, only found in two-mica granites, indicates the involvement of biotite during melting, and this is consistent with the more mafic features of the two-mica granite (higher Mg, Ti, Fe, Sr, Y, Zr, Ba and REE) with respect to tourmaline granite (Holtz and Johannes, 1991; Icenhower and London, 1995, Acosta-Vigil et al., 2010). Petrographic evidence for the peritectic origin of the cordierite, according to the reaction sill+bt=cord+melt, was reported by Visonà and Lombardo (2002). The high content of Na_2O (up to 1.52 wt%, Tab. 4) and the abundance of channel cations (Ca, Na, K; Tab. 4) of euhedral cordierite also suggests its crystallisation in the presence of silicate melts (Pereira and Bea, 1994; Clarke, 1995; Alasino et al., 2010).

6.1.2 Composition of b*iotite and muscovite*

The microstructures are similar to those described in the literature for magmatic muscovite (Miller et al., 1981; Zen, 1988). In the unfoliated two-mica granite, the mineral chemistry of both

biotite and muscovite is compatible with their crystallisation from a magma (D_{Ti}^{Bt-Ms} mean 4.51±2.3). The high contents of alumina in the biotite of all samples (Al^{IV}=2.68±0.07) imply the presence of an Al-rich phase (e.g. andalusite) saturating alumina in the magma already during the crystallisation of biotite (Clarke et al., 2005). Therefore, the microstructures and composition of micas indicate that andalusite is not a late-crystallising mineral but probably constitutes an early phase in the magma.

6.1.3 Microstructures of andalusite.

The variety of microstructures in which andalusite is found, in cases within the same sample, can be explained as due to different origins (e.g., metamorphic or magmatic) and/or to crystallization from the magma at different stages (Clarke et al., 2005).

Single-crystal grains (S). This type of euhedral to subhedral andalusite, included in plagioclase cores or size-compatible in the matrix, with or without a muscovite mantle, is probably magmatic (i.e., magmatic-peritectic and/or magmatic-cotectic), and the crystals owe their shape to the fact that they grew freely in the melt. Euhedral andalusite (lacking a muscovite mantle) in plagioclase (Fig. 3a, b, g) may represent one of the first minerals present in a melt either saturated in Al_2SiO_5 from the source, or in which Al_2SiO_5 saturation occurred (e.g., ASI ≥ 1.15; Acosta-Vigil et al, 2003; Clarke et al., 2005). It is also possible that these crystals represent peritectic andalusite (crystallised during a peritectic reaction of the type mu+qtz+ab = and+melt) as suggested by inclusions of andalusite + quartz grains in plagioclase cores (Fig. 3b). With respect to the andalusite-sillimanite stability field boundary proposed by Pattison (1992), the peritectic reaction mu+qtz+ab = Al_2SiO_5+melt falls in the sillimanite field (Fig. 6). However, the andalusite-sillimanite boundary after Richardson (1969) occurs at a higher temperature at constant pressure (R69 in Fig. 6) and, in this case, the formation of peritectic andalusite would have been possible. Either crystallised together with the melt (peritectic) or from the melt (cotectic), these microstructures suggest that andalusite is not a late-crystallising phase, but was present early in the history of the leucogranitic magma. Euhedral andalusite may also crystallise later, as a consequence of late Al_2SiO_5 saturation in the melt. This may be the case of the cm-sized pecilitic andalusite associated with dumortierite in the Zemu valley pegmatitic leucogranite, which perhaps resulted from growth in a water-saturated melt (e.g., Whitney and Dilek, 2000; Clarke et al., 2005). Single anhedral grains of andalusite in plagioclase (e.g., sample V731 in Fig 3c) may result from a reaction between an andalusite of any origin (residual, peritectic or early magmatic) with the silicate melt phase (Clarke et al., 2005). In particular, it is more probable that andalusite is residual in cases such

as that of sample V731, in which plagioclase also contains other residual minerals such as prismatic sillimanite and corundum. Microstructures of overgrowths of sillimanite after andalusite (residual or peritectic) like that shown in Fig. 3l suggest an increase in temperature after andalusite crystallisation. The overgrowth of a magmatic muscovite mantle (with Na/(Na+K)>0.06) on andalusite in the matrix is interpreted as a reaction during cooling between the residual magma and andalusite at low pressure (below 400 MPa), in the stability field of muscovite.

Clustered grains (C). The existence of the size-incompatible (small) clustered andalusite grains leads to at least two different interpretations. In the interstitial clusters of euhedral to subhedral andalusite (sample V471, Fig. 3i) the crystals may have grown in the free spaces between the larger crystals which formed earlier, in which case the muscovite of their mantle would represent the last magmatic mineral to form. These microstructures are interpreted as result from late cotectic crystallization of andalusite in a magma saturated in Al_2SiO_5. Sample V471 also shows anhedral andalusite included in plagioclase, which may indicate that the magma was saturated or close to saturation in Al_2SiO_5 during its early history, and probably throughout its history. The clusters of optically discontinuous rounded grains of different sizes included in biotite or plagioclase (e.g., sample V93, Fig. 2e) cannot be interpreted as quenched crystals formed during late crystallization of the magma. Instead, the inclusion of this type of cluster in early-crystallised silicates is consistent with a hypothesis of refractory residues. Experiments show that, at low pressure (e.g., 200-500 MPa), pelite is the most fertile rock, producing melts with andalusite residues (Thompson, 1996), the solubility of which in crustal melts is limited by the relatively low temperatures and, to lower extent, water contents (Acosta-Vigil et al., 2003). In conclusion, these clusters may represent concentrations of refractory residues in a partial melting scenario.

To summarise, the andalusite in single anhedral crystals included in plagioclase, those forming the clusters of packed crystals included totally or only partially in plagioclase and biotite, and those wrapped within sillimanite are all interpreted here as of probable residual origin. The single euhedral andalusite crystals included in plagioclase or interstitial probably have a peritectic or early cotectic origin. The interstitial clusters of euhedral to subhedral andalusite represent cotectic crystallisation in a magma saturated in Al_2SiO_5.

6.2 Conditions of anatexis

Most of the samples contain residual and/or magmatic (early and/or late) cotectic andalusite (e.g. sample V471), indicating that the whole P-T path from anatexis to melt solidification occurred at $P \leq$ about 400 MPa **(**P92 triple point, Fig. 6**).** Considering the maximum pressure for andalusite stability and the location of the wet granite solidus, the minimum temperature indicated by the

formation of peritectic cordierite + melt, from sillimanite + biotite, is ~ 660-700 °C (Fig. 6). Temperatures up to 798 °C, obtained for the andalusite two-mica granite according to the concentrations of Zr and REE in the leucogranite (Tab. 6), probably represent an estimate of the maximum temperature of magma at its source (Miller et al., 2003). However, these T values may also be overestimated, due to the widespread occurrence of inherited zircon and monazite (e.g. Streule et al., 2010). At the temperatures suggested by Qtz-Or-Ab normative compositions and accessory thermometry, and in the presence of andalusite, the high ASI of the leucogranites suggests that the melt was relatively rich in water (Acosta-Vigil et al., 2002; 2003). Compared with the heating path, during cooling and crystallization of the magma, the pressure either remained constant or underwent a slight decrease, with a cooling path approximately parallel to that during prograde anatexis, as shown by the presence of andalusite throughout the history of the magma and by the formation of magmatic muscovite (Thompson and Algor, 1977; Clarke et al., 2005). The excess of alumina and the relatively high amounts of B and F in the melt (occurrence of tourmaline and fluorite, Visonà and Lombardo, 2002; replacements/overgrowths of cordierite by late tourmaline, this paper) probably decreased the temperature of the granite solidus with respect to that of H_2O-saturated haplogranite melts (Manning, 1981; Pichavant, 1987; Holtz et al.,1992a, b; London, 1992). Consequently, the fields of magmatic andalusite and muscovite of the granite examined here extended towards lower P and T values. Fig. 6 shows the likely solidus of the andalusite leucogranite magmas during crystallisation (dashed curve in Fig. 6). Otherwise, later magmatic andalusite and muscovite, observed in the studied granites would not have formed.

The leucogranites examined here also commonly contains sillimanite, which may be either residual, magmatic (Visonà and Lombardo, 2002) or post-magmatic and subsolidus (Musumeci, 2002; Kellett et al., 2009). The acicular sillimanite overgowth on andalusite (Fig. 3l) is interpreted as a record of the prograde heating which caused dehydration melting of biotite in the sillimanite field (Fig. 6). In the foliated granites (e.g., sample 18d, Makalu), fibrous sillimanite is found in heterogeneous shear zones in which it is "disharmonious" (*sensu* Vernon and Flood, 1977) with respect to the muscovite in the foliation. In this case, as proposed for the neighbouring leucogranite of the Everest valley (Musumeci, 2002), the growth of sillimanite is subsolidus and results from the formation of heterogeneous shear zones. In unfoliated leucogranite (e.g., V472 and VS38), the brown fibrous sillimanite along the mineral junctions of the matrix (Fig 3a, e, f) is interpreted as the product of protonic hydrolysis (base-cation leaching; Vernon, 1987). According to this hypothesis, the agents responsible for leaching were not magmatic fluids, because they were already alkali-saturated, but probably metamorphic aqueous fluids. The unoriented acicular sillimanite replacing muscovite and biotite (e.g., sample V730, Fig. 3n) might represent the effects of a thermal event

409 which took place after the leucogranite solidification. However, in the absence of any other
410 geological data supporting this interpretation, Kellett et al. (2009) suggested that, in the andalusite-
411 bearing leucogranite of Bhutan, sillimanite grew in the andalusite field during magma cooling. In
412 this context, the expansion of sillimanite stability towards lower temperatures requires the presence
413 of magmatic fluids, and not metamorphic, with particular concentrations in transition metals
414 (Grambling and Williams, 1985; Pattison, 1992), but no evidence of such fluids was found
415 (andalusite contains negligible concentrations of transition elements; Tab. 5). Alternatively, this
416 type of retrograde sillimanite may result from to a thermal event locally associated with
417 heterogeneous shear zones, like that of the Everest valley leucogranite.
418
419 **6.3 Implications for the Himalaya orogeny**
420 The genesis of the andalusite leucogranites studied here is consistent with anatexis of
421 metapelite during low-pressure prograde heating. This does not seem to match either original or
422 currently proposed geodynamic models (e.g., extrusion and channel flow) that imply the generation
423 of all the Himalayan leucogranite during decompression melting of the HHC (e.g., Harris et al.,
424 1993; Patiño-Douce and Harris, 1998; Searle et al., 2010). The P-T evolution of the Himalayan
425 metamorphism in the upper HHC (Barun gneiss, north of the High Himalayan Thrust – HHT in Fig
426 1) of the Everest region and, further north, in the Mabjia dome (North Himalaya) is relatively well
427 constrained, with an early prograde Barrovian event occurring at ~ 32-39 Ma and a later event at ~
428 25-16 Ma (Lee and Whitehouse 2007; Jessup et al., 2008; Cottle et al., 2009b; M1 to M3 events of
429 Pognante and Benna, 1993). During this time interval, with P diminishing from 600 to 400 MPa,
430 there were two stages of migmatization and of magma production, at ~24 Ma and < 16 Ma,
431 associated with the extrusion of the HHC (Simpson et al., 2000; Viskupic et al., 2005; Lee and
432 Whitehouse 2007; Jessup et al., 2008; J. M. Cottle et al., 2009b; Streule et al., 2010). In this
433 hypothesis of decompression melting of the HHC, andalusite may only form from the magma after
434 its emplacement at the shallowest levels. The migmatitic stage which terminated at ~16 Ma is
435 considered to represent the end of the south-directed channel flow (Murphy and Harrison, 1999;
436 Cottle et al., 2009b; Streule et al., 2010). This second metamorphic event coincides in time and P-T
437 conditions with the data derived from the andalusite leucogranites. Thus, the P-T estimates record a
438 decrease in pressure to 300-200 MPa (Jessup et al., 2008; Streule et al., 2010), compatible with the
439 growth of andalusite described in the structurally higher metapelitic levels of the HHC and in those
440 at the base of the Everest Series (Palivcova et al., 1982; Pognante and Benna, 1993; Jessup et al.,
441 2008). Also, in the Makalu pluton, two phases of granite emplacement have yielded ages of 24-21
442 Ma (Schärer et al., 1986; Streule et al., 2010) and 15.7 Ma (Streule et al., 2010), which coincide

443 with the two main stages of migmatisation recorded in the HHC rocks (see above). The studied
444 andalusite leucogranite, which composes the higher part of this pluton (sampled at 7075 m), yields
445 an age of 15.9 ± 0.4 Ma, which is statistically equivalent to that reported by Streule et al. (2010) for
446 the younger granitic pulse. These two ages also coincide with that of anatexis of 16.0±0.6 Ma
447 (Streule et al., 2010) in the HHC immediately underlying the pluton, in which andalusite has been
448 found in leucosomes (Pognante and Benna, 1993). The P and T conditions at the end of
449 crystallisation in them and in the granite have values of about 200 MPa and 600 °C, and are viewed
450 as constraining the clockwise P-T path from high-temperature to low-pressure metamorphism
451 (Streule et al., 2010). These values, however, are not compatible with the formation of magmatic
452 andalusite and muscovite in the leucogranite of the highest part of the Makalu pluton. Lastly, and in
453 general, despite all the above coincidences in age and P-T conditions, there is one major problem,
454 this andalusite leucogranite was probably generated at low pressure, and this is not compatible with
455 the metamorphic evolution recorded in the HHC rocks (e.g. Groppo et al., 2012). Therefore, in the
456 Everest-Makalu-Kharta area, the previously documented clockwise P-T path metamorphism in the
457 extruding HHC could not have generated the andalusite leucogranite, because its formation requires
458 low-pressure anatectic metamorphism of prograde character.
459 The occurrence of two types of leucogranites showing melting at intermediate pressure
460 (originated by decompression; e.g., Searle et al., 2010, and references therein) and low pressure
461 (formed by isobaric heating; this paper) may be explained in the following way. Because melting
462 during heating at low pressure requires an extra input of heat (as documented by petrological data),
463 this implies that hotter material (from below) came into contact with the source rocks of the
464 andalusite leucogranites. The rocks above the andalusite-bearing leucogranite would be excluded,
465 as they record a lower metamorphic grade with respect to the HHC rocks. One possibility is that
466 normal faults/shear zones have put into contact colder rocks above and hotter rocks below.
467 However, most authors agree that the general tectonic setting active during the exhumation and/or
468 extrusion of the HHC was compressional. The contemporaneous activity of the upper STDS and
469 lower MCT, bordering the HHC, drove the high- to medium-grade metamorphic rocks of the HHC
470 to higher structural levels (Godin et al., 2006, and references therein).Taking into account two of
471 the most popular models of exhumation of the HHC, such as extrusion and channel flow, we must
472 consider that rocks are exhumed in a general flow derived from the combination of simple and pure
473 shear components acting together (Law et al., 2004; Carosi et al., 2006, 2007). The
474 contemporaneous activity of pure and simple shear components determines the parabolic shape of
475 the velocity profiles of material particles moving across a vertical section through the HHC so that,
476 schematically, particle velocities are higher in the middle of the tectonic unit and decrease towards

its boundaries (Godin et al., 2006; Grujic, 2006). A consequence is that hot rocks in the middle of the HHC moved faster than the rocks above (and below) them, so that, after some millions of years, hotter rocks from the middle part of the HHC may came into contact with the colder rocks above (Fig. 7). In such a way, the hotter rocks may have generated an additional input of heat towards the relatively colder muscovite-bearing rocks above, causing them to melt during prograde heating at lower pressure and produce andalusite-bearing leucogranites. An increase of temperature at low pressure is compatible with the occurrence of late andalusite in the schists of the Everest valley (Jessupp et al., 2008), in those of the high Barun valley (Palivcova et al., 1982; Pognante and Benna, 1993) and in the Ama Drime paragneissic unit (Kali et al., 2010). The interpretation that this andalusite represents a product of the metamorphic reaction at the end of the P-T clockwise decompression path is only acceptable for the Nupse-Lhotse pelite (Everest schists), which contain muscovite, but not for the other two cases (HHC pelite) in which mica must already have been consumed at higher temperatures during the decompressive anatectic phase. We therefore emphasise that, for the complete understanding of the orogenic evolution of the belt, several mechanisms for the generation of granite generation and, correspondingly, occurrence of two different P-T paths must be taken into account.

The occurrence of the younger andalusite-bearing leucogranite is compatible with the channel flow or general extrusion models proposed for the HHC, but it is not enough to discriminate between the two models (Carosi et al., 2006, 2010). In any case, the available structural and kinematic data (Carosi et al., 2006, 2010) currently reveal no evidence of extensional faults or shear zones, and support the hypothesis of exhumation in a general compressive tectonic setting.

7. Conclusions

Andalusite-bearing leucogranites outcrop in a well-defined area in the central-eastern sector of the Himalayan belt. The residual and/or magmatic peritectic origin of andalusite in most of the studied leucogranites constrains anatexis at low pressure conditions during prograde heating. The age of 16 Ma obtained from the upper portion of the Makalu leucogranite links the generation of andalusite-bearing leucogranites with the most recent anatectic-metamorphic event documented in the area.

Dehydration melting of muscovite during heating and/or decompression of the HHC, often invoked as a suitable mechanism for the generation of the Himalayan leucogranites, took place in the sillimanite field and thus cannot explain the production of leucogranites at low pressure ($P <$ about 400 MPa). P and T conditions for anatexis in the andalusite field could only have taken place at higher structural levels, and with the input of some extra heat. This input of heat may have been

caused by the exhumation of the HHC by non-coaxial deformation (e.g., simple shear + pure shear). In this model, the path of particles during exhumation was parabolic in shape, and the more exhumed (and hotter) portion occurred in the middle portion of the HHC (Fig. 7). The more exhumed central and hotter parts of the HHC may have come into contact with the upper and colder parts, made of fertile lithologies. In this way, if during exhumation the velocity of displacement parallel to the tectonic boundaries did not overcome the velocity of heat conduction (nearly perpendicular to tectonic boundaries), the higher part of the HHC would have received enough heat to produce (new) anatexis and the formation of subsolidus sillimanite in the already generated granite.

In conclusion, a simple decompression model is not appropriate to explain the occurrence of andalusite-bearing leucogranites. Two events of anatexis, in the sillimanite and andalusite stability fields, respectively, are necessary to explain the generation of all the leucogranites outcropping in the HHC and north Himalayan domes.

Acknowledgements

This research was funded by the Universities of Padova (V.D.) and Pisa (R.C., C.M.), PRIN Cofin 2006. We wish to thank A. Acosta-Vigil and D. B. Clarke, who greatly improved the manuscript with their constructive criticism and helpful suggestions, P. Pertusati for lively discussions in the field and for sharing his knowledge of metamorphic structures and rocks. Mineral analyses were acquired in the electron microprobe laboratories of the Department of Earth Sciences, University of Padova. We would also like to thank the guide Diego Fregona for collecting samples and geological pictures along the "French path" during the Italian Makalu expedition in 2002 (Barun base camp – Maklalu La-Summit Makalu). The English version of the Italian text was translated by Gabriel Walton.

REFERENCES

van Achterbergh, E., Ryan, C.G., Jackson, S.E., Griffin, W., 2001. Data reduction software for LA-ICP-MS. In: Sylvester, P. (ed.) Laser Ablation-ICPMS in the Earth Sciences. Mineralogical Association of Canada, Short Course Series 29, 239-243.

Acosta-Vigil, A., Pereira, M.D., Shaw, D.M, London, D., 2001. Contrasting behavior of B during crustal anatexis. Lithos 56, 15-31.

Acosta-Vigil, A., London, D., Dewers, T.A., Morgan VI, G.B., 2002. Dissolution of corundum and andalusite in H2O-saturated haplogranitic melts at 800 °C and 200 MPa: constraints on diffusivities and the generation of peraluminous melts. Journal of Petrology 43, 1885-1908.

Acosta-Vigil, A., London, D., Morgan VI, G.B., Dewers, T.A., 2003. Solubility of excess alumina in hydrous granitic melts in equilibrium with peraluminous minerals at 700-800 °C and 200

MPa, and applications of the aluminum saturation index. Contributions to Mineralogy and Petrology 146, 100-119.

Acosta-Vigil, A., London, D., Morgan VI, G.B., 2006. Experiments on the kinetics of partial melting of a leucogranite at 200MPa and 690-800 °C: compositional variability of melts during the onset of H_2O-saturated crustal anatexis. Contributions to Mineralogy and Petrology 151, 539-557.

Acosta-Vigil A., Buick, I., Hermann, J., Cesare, B., Rubatto, D., London, D., Morgan VI, G.B., 2010. Mechanisms of crustal anatexis; a geochemical study of partial melted metapelitic enclaves and host dacite, SE Spain. Journal of Petrology 51, 785-821.

Alasino, P.H., Dahlquist, J.A., Galindo, C., Casquet, C., Saavedra, J., 2010. Andalusite and Na- and Li-rich cordierite in the La Costa pluton, Sierra Pampeanas, Argentina: textural and chemical evidence for a magmatic origin. International Journal of Earth Science 99, 1051-1065.

Beaumont, C., Jamieson, R.A., Nguyen, M.H., Lee, B., 2001. Himalayan tectonics explained by extrusion of a low-viscosity crustal channel coupled to focused surface denudation, Nature 414, 738–742, doi:10.1038/414738a.

Bordet, P., 1961. Recherches géologiques dans l'Himalaya du Nepal, région du Makalu. Editions du Centre National de la Recherche Scientifique, Paris, 275 pp.

Borghi, A., Castelli, D., Lombardo, B.,Visona', D., 2003. Thermal and baric evolution of garnet granulites from the Kharta region of S Tibet, E Himalaya. European Journal of Mineralogy 15(2), 401-418.

Brigatti, M.F., Frigieri, P., Ghezzo, C., Poppi, L., 2000. Crystal chemistry of Al-rich biotites coexisting with muscovites in peraluminous granites. American Mineralogist 85, 436–448.

Burchfiel, B.C., Chen, Z., Hodges, K.V., Liu, Y., Royden, L.H., Deng, C., Xu, J., 1992. The South Tibetan Detachment System, Himalayan Orogen: extension contemporaneous with and parallel to shortening in a collisional mountain belt. The Geological Society of America Special Paper 269, 41 pp.

Carosi, R., Montomoli, C., Rubatto, D., Visona', D., 2006. Normal-sense shear zones in the core of the Higher Himalayan Crystallines (Bhutan Himalayas): evidence for exstrusion? In: Law, R.D., Searle, M., Godin, L. (Eds.), Channel Flow, Ductile Extrusion and Exhumation of Lower-mid Crust in Continental Collision Zones. Geological Society of London, Special Pubblication 268, 425-444.

Carosi, R., Montomoli, C., Visona', D., 2007. A structural transect in the Lower Dolpo: Insights on the tectonic evolution of Western Nepal. Journal of Asian Earth Sciences, 29, 407-423.

Carosi, R., Montomoli, C., Rubatto, D., Visona', D., 2010. Late Oligocene high-temperature shear zones in the core of the Higher Himalayan Crystallines (Lower Dolpo, Western Nepal). Tectonics, 29: TC4029, doi:10.1029/2008TC002400.

Castelli, D., Lombardo, B., 1988. The Gophu La and Western Lunana granites: Miocene muscovite leucogranites of the Bhutan Himalaya. Lithos 21, 211 – 225.

Clarke, D.B., 1995. Cordierite in felsic igneous rocks: a synthesis. Mineralogical Magazine 59, 311 – 325.

Clarke, D.B., Dorais, M., Barbarin, B., Barker, D., Cesare, B., Clarke, G., el Baghdadi, M., Erdmann, S., Förster, H-J., Gaeta, M., Gottesmann, B., Jamieson, R.A., Kontak, D.J., Koller, F., Gomes, C.L., London, D., Morgan VI, G.B., Neves, L.J.P.F., Pattison, D.R.M., Pereira, A.J.S.C., Pichavant, M., Rapela, C., Renno, A.D., Richards, S., Roberts, M., Rottura, A., Saavedra, J., Sial, A.N., Toselli, A.J., Ugidos, J.M., Uher, P., Villaseca, C., Visonà, D., Whitney, D.L., Williamson, B., Woodard, H.H., 2005. Occurrence and origin of andalusite in peraluminous felsic igneous rocks. Journal of Petrology 46, 441–472. doi: 10.1093/petrology/egh083.

Clarke, D.B., 2007. Assimilation of xenocrysts in granitic magmas: Principles, processes, proxies, and problems. The Canadian Mineralogist Vol. 45, 5-30.

598 Clarke, D.B., Wunder, B., Förster , H.J., Rhede, D., Hahn, A., 2009. Experimental investigation of
599 near-liquidus andalusite-topaz relations in synthetic peraluminous haplogranites at 200 MPa.
600 Mineralogical Magazine 73(6), 997–1007.
601 Cottle, J.M., Jessup, M.J.; Newell, D.L.. Horstwood, M.S.A., Noble, S.R.; Parrish, R.R., Waters, D.
602 J., Searle, M.P., 2009*a*. Geochronology of granulitized eclogites from the Ama Drime Massif,
603 implications for the tectonic evolution of the South Tibetan Himalaya. Tectonics 28:TC1002.
604 Cottle, J.M., Searle, M.P., Horstwood, M.S.A., Waters, D., 2009*b*. Timing of midcrustal
605 metamorphism, melting, and deformation in the Mount Everest region of southern Tibet
606 revealed by U(-Th)-Pb geochronology. Journal of Geology 117, 643–664.
607 Debon, F., Le Fort, P., 1983. A chemical– mineralogical classification of common plutonic rocks
608 and associations: principles, methods, applications. Bulletin de Mineralogie 111, 493– 510.
609 Debon, F., Le Fort, P., Sheppard, S.M., Sonet, J., 1986. The four plutonic belts of the
610 Transhimalaya-Himalaya: a chemical, mineralogical, isotopic, and chronological synthesis
611 along a Tibet-Nepal section. Journal of Petrology 27(1), 219-250.
612 Dèzes, P., 1999. Tectonic and metamorphic evolution of the Central Himalayan domain in
613 Southeast Zanskar (Kashmir, India). Mémoires de Géologie (Lausanne) 32, 145pp.
614 Gansser, A., 1964. Geology of the Himalayas. Wiley-Interscience, London.
615 Godin, L., Grujic, D., Law, R.D., Searle, M.P., 2006. Channel flow, ductile extrusion and
616 exhumation in continental collision zones: An introduction, in: Law, R.D., Searle, M.P.,
617 Godin, L. (Eds.), Channel Flow, Ductile Extrusion and Exhumation in Continental Collision
618 Zones. Geological Society, London, Special Publication 268, 1–23.
619 Grambling, J.A., Williams, M.L., 1985. The effects of Fe^{3+} and Mn^{3+} on aluminum silicate phase
620 relations in north-central New Mexico, U.S.A.: Journal of Petrology 26(2), 324-354.
621 Groppo, C., Rolfo, F., Indares, A., 2012. Partial melting in the Higher Himalayan Crystallines of
622 Eastern Nepal: the effect of decompression and implications for the 'Channel Flow'model.
623 Journal of Petrology, 1-32, doi:10.1093/petrology/egs009.
624 Grujic, D., 2006. Channel flow and continental collision tectonics; an overview, in: Law, R.D.,
625 Searle, M.P., Godin, L. (Eds.), Channel Flow, Ductile Extrusion and Exhumation in
626 Continental Collision Zones. Geological Society, London, Special Publication, 268, 25-37.
627 Guillot, S., Le Fort, P., 1995. Geochemical constraints on the bimodal origin of High Himalayan
628 leucogranites. Lithos 35, 221–234.
629 Harris, N., Inger, S. and Massey, J. (1993). The role of fluids in the of High Himalayan
630 leucogranites. In: Searle, M., P., Treloar, P., J., (eds) *Himalayan Tectonics. Geological*
631 *Society, London, Special Publication* **74,** 391–400.
632 Holtz, F., Johannes, W., 1991. Genesis of peraluminous granites: I. Experimental investigation of
633 melt compositions at 3 and 5 kb and various H2O activities. Journal of Petrology 32, 935–
634 958.
635 Holtz F, Johannes W, Pichavant M (1992a) Peraluminous granites: the effect of alumina on melt
636 composition and coexisting minerals. Transactions of the Royal Society of Edinburgh: Earth
637 and Environmental Science, 83:409–416
638 Holtz F, Johannes W, Pichavant M (1992b) Effect of excess aluminum on phase relations in the
639 system Qz-Ab-Or. Experimental investigation at 2 kbar and reduced H2O activity. European
640 Journal of Mineralogy, 4, 137–152
641 Jessup, M.J., Cottle, J.M., Searle, M.P., Law, R.D., Newell, D.L., Tracy, R.J., Waters, D.J., 2008.
642 P-T-t-D paths of Everest Series schists, Nepal. Journal of Metamorphic Geology 26, 717-
643 739.
644 Kali, E., Leloup, P.H., Arnaud, N., Mahéo, G., Liu, D., Boutonnet, E.,Vanderwoerd, J., Liu X., Jing
645 Liu‐Zeng, Haibing Li, 2010. Exhumation history of the deepest central Himalayan rocks, Ama
646 Drime range: Key pressure-temperature-deformation-time constraints on orogenic models
647 Tectonics, 29; TC2014, doi:10.1029/2009TC002551.

Kellett, D.A., Grujic, D., Erdmann, S., 2009. Miocene structural reorganization of the South Tibetan detachment, eastern Himalaya: Implications for continental collision. Lithosphere, 1(5), 259-281.

Ketchum, J.W.F., Jackson, S.E., Culshaw, N.G., Barr, S.M., 2001. Depositional and tectonic setting of the Paleoproterozoic Lower Aillik Group, Makkovik Province, Canada: evolution of a passive margin-foredeep sequence based on petrochemistry and UPb (TIMS and LAM-ICP-MS) geochronology. Precambrian Research 105, 331-356.

Kretz, R., 1983. Symbols for rock-forming minerals. American Mineralogist 68, 277–279.

Icenhower, J.P., London, D., 1995. An experimental study of element partitioning among biotite, muscovite, and coexisting peraluminous silicic melt at 200 MPa (H2O). American Mineralogist 80, 1229–1251.

Larson, K.P., Godin, L., Davis, W.J., Davis, D.W., 2010. Out-of-sequence deformation and expansion of the Himalayan orogenic wedge: insight from the Changgo culmination, south central Tibet. Tectonics, 29: TC4013, doi:10.1029/2008TC002393.

Law, R.D., Searle, M.P., Simpson, R.L., 2004. Strain, deformation temperatures and vorticity of flow at the top of the Greater Himalayan Slab, Everest Massif, Tibet. Journal of the Geological Society 161, 305–320.

Le Fort, P., 1975. Himalayas: the collided range. Present knowledge of the continental arc. American Journal of Science, 275-a: 1-44.

Lee, J., Hacker, B., Wang, Y., 2004. Evolution of North Himalayan gneiss domes: structural and metamorphic studies in Mabja Dome, southern Tibet. Journal of Structural Geology, 26(12), 2297-2316.

Lee, J., McClelland, W., Wang, Y., Blythe, A., McWilliams, M.O., 2006. Oligocene-Miocene middle crustal flow in southern Tibet: geochronology of Mabja Dome. In: Law, R. D., Searle, M. P., Godin, L. (Eds.), Channel Flow, Ductile Extrusion and Exhumation in Continental Collision Zones. Geological Society, London, Special Publications 74, 445-469.

Lee, J., Whitehouse, M. J., 2007. Onset of mid-crustal extensional flow in southern Tibet: Evidence from U/Pb zircon ages. Geology 35,45-48.

London, D., 1992. The application of experimental petrology to the genesis and crystallization of granitic pegmatites. Canadia Mineralogist, 30, 499-540.

Ludwig, K.R., 2000. Isoplot a geochronological toolkit for Microsoft Excel. Berkeley Geochronology Center, Special Publications 1a, 53 p.

Manning, D., A., C., 1981. The effect of fluorine on liquidus phase relationships in the system Qz-Ab-Or with excess water at 1 kb. Contribution to Mineralogy and Petrology, 76, 206-215.

Miller, C.F., Stoddard, E.F., Bradfish, L.J., Dollase, W.A., 1981. Composition of plutonic muscovite: genetic implications. The Canadian Mineralogist 19, 25-34.

Miller, C.F., McDowell, S.M., Mapes, R.W., 2003. Hot and cold granites? Implications of zircon saturation temperatures and preservation on inheritance. Geology 31, 529-532.

Monier, G., Mergoil-Daniel, J., Labernardiere, H., 1984. Generations successives de muscovites et feldspaths potassiques dans les leucogranite du massif de Millevaches (Massif Central francais). Bulletin de Mineralogie 107, 55–68.

Mosca, P., Groppo, C. Rolfo, F., 2010. Structural and metamorphic architecture of the Himalayas in the Kangchenjunga area (far-Eastern Nepal). Rendiconti on line, II, 423-424.

Murphy, M., Harrison, T.M., 1999. Relationship between leucogranites and the Qomolangma detachment in the Rongbuk Valley, south Tibet. Geology 27, 831– 834.

Musumeci, G., 2002. Sillimanite-bearing shear zones in syntectonic leucogranite: fluid- assisted brittle-ductile deformation under amphibolites facies conditions. Journal of Structural Geology 24, 1491-1505.

Palivcova, M., Kalvoda, J., Minarik, L., 1982. Petrology of the Makalu massif, Nepal Himalayas. Rozpr. Cesk. Akad.Ved 92 (2), 1 – 69.

Patiño-Douce, A., Harris, N., 1998. Experimental constraints on Himalayan anatexis. Journal of Petrology, 39, 689– 710.

Pattison, D.R.M., 1992. Stability of andalusite and sillimanite and the Al2SiO5 triple point: constraints from the Ballachulish aureole, Scotland. Journal of Geology 100, 423– 446.

Pereira , M.D., Bea, F., 1994. Cordierite-producing reactions in the Peña Negra Complex, Avila batholith, Central Spain: the key role of cordierite in low-pressure anatexis. The Canadian Mineralogist, 32, 763-780.

Pichavant, M., 1987. Effect of B and H_2O on liquidus phase relations in the haplogranitic system at 1 kbar. American Mineralogist, 72, 1056-1070.

Pognante, U., Benna P., 1993. Metamorphic zonation, migmatization, and leucogranites along the Everest transect of Eastern Nepal and Tibet: record of an exhumation history. *in*: Treloar, P.J., Searle, M.P., (Eds), Himalayan Tectonics,. Geological Society of London Special Publication, **74**, 323- 340.

Richardson, S.W., Gilbert, M.C., Bell, P.M., (1969). Experimental determination of kyanite – andalusite and andalusite–sillimanite equilibria; the aluminum silicate triple point. American Journal of Science 267, 259–272.

Rolfo, F., Carosi, R., Montomoli, C., Visonà, D., Villa, I. M., 2006. A geological transect east of Kangchendzonga (North Sikkim, India). Journal of Asian Earth Sciences, 26: 158.

Schärer, U., Xu, R. H., and Allegre, C.J., 1984. U-Pb geochronology of Gandese (Transhimalaya) plutonism in the Lhasa-Xigaze region, Tibet. Earth and Planetary Science Letters, 69, 311-320.

Schärer, U., Xu, R-H, and Allègre, C.J., 1986. U-(Th)-Pb systematics and ages of Himalayan leucogranites, South Tibet. Earth and Planetary Science Letters, 77, 35-48.

Searle, M.P., Cottle, J.M., Streule, M.J., Waters, D.J., 2010. Earth and Environmental Science Transactions of the Royal Society of Edinburgh 100, 219-233.

Simpson, R.L., Parrish, R.R., Searle, M.P, Waters, D.J., 2000. Two episodes of monazite crystallization during metamorphism and crustal melting in the Everest region of the Nepalese Himalaya. Geology 28, 403-406.

Sláma, J., Košler, J., Condon, D.J., Crowley, J.L., Gerdes, A., Hanchar, J. M., Horstwood, M.S.A., Morris, G.A., Nasdala, L., Norberg, N., Schaltegger, U., Schöne, B., Tubrett, M. N., Whitehouse, M.J., 2008. Plešovice zircon — A new natural reference material for U–Pb and Hf isotopic microanalysis. Chemical Geology 249, 1-35.

Streule. M.J., Searle, M.P., Waters, D.J., Matthew, S.A., Horstwood, M.S.A., 2010. Metamorphism, melting and channel flow in the Greater Himalaya Sequence and Makalu leucogranite: constraints from thermobarometry, metamorphic modelling and U-Pb geochronology. Tectonics 29: TC5011, doi:10.1029/2009TC002533.

Thompson, A.B., Algor, J.R., 1977. Model systems for anatexis of pelitic rocks Contributions to Mineralogy and Petrology 63, 247-269.

Thompson, A.B., 1996. Fertility of crustal rocks during anatexis. Transactions of Royal Society of Edinburgh: Earth Sciences 87, 1-10, 1996.

Tiepolo, M., 2003. In situ Pb geochronology of zircon with laser ablation-inductively coupled plasma-sector field mass spectrometry. Chemical Geology 199 159-177.

Vernon, R.H., and Flood, R.H., 1977. Interpretation of metamorphic assemblages containing fibrolitic sillimanite. Contributions to Mineralogy and Petrology. 59, 277-235.

Vernon, R.H., 1987. Formation of late sillimanite by hydrogen metasomatism (base leaching) in some high grade gneisses. Lithos 79, 143-152.

Viskupic, K., Hodges, K.V., Bowring, S.A., 2005. Timescales of melt generation and the thermal evolution of the Himalayan metamorphic core, Everest region, eastern Nepal, Contributions to Mineralogy and Petrology 149(1), 1–21.

Visonà, D., Lombardo, B., 2002. Two mica- and tourmaline leucogranites from the Everest-Makalu region (Nepal-Tibet). Himalayan leucogranite genesis by isobaric heating? Lithos 62(3-4): 125-150.

White, R.W., Powell, R., Holland, T.J.B., 2001. Calculation of partial melting equilibria in the system Na2O–CaO–K2O–FeO–MgO–Al2O3–SiO2–H2O (NCKFMASH). Journal of Metamorphic Geology 19 (2), 139–53.

Whitney, D.L., Dilek, Y., 2000. Andalusite–sillimanite–quartz veins as indicators of low-pressure–high-temperature deformation during late-stage unroofing of a metamorphic core complex, Turkey. Journal of Metamorphic Geology 18, 59–66.

Zhang, H., Harris, N., Parrish, R.R., Kelley, S., Zhang, L., Rogers, N., Argles, T., King, J., 2004. Causes and consequences of protracted melting of the mid-crust exposed in the North Himalayan antiform. Earth and Planetary Science Letters 228(1-2): 195-212.

Zen, E-an, 1986. Aluminium enrichment in silicate melt by fractional crystallization: some mineralogic and petrographic constraints. Journal of Petrology 27, 1095-1117.

Zen, E-an, 1988. Phase relations of peraluminous granitic rocks and their petrogenetic implications. Annual Review of Earth and Planetary Sciences 16, 21–51.

CAPTIONS

Fig 1. Simplified geological map of central (-east) Himalayan range from Gansser (1983), Burchfiel et al. (1992), with modifications by Grujic et al. (2002) and Cottle et al (2007). High Himalayan Thrust (HHT) divides upper from lower structural level of HHC. Stars: locations of Miocene leucogranite with andalusite known in literature: 1, Debon et al. (1986); 2 and 3, Zhang et al. (2004); 4, Palivcova et al. (1982), Pognante and Benna (1993); 5, Mosca et al. (2010); 6, Rolfo et al. (2006); 7, Kellett et al. (2009); 8, Castelli and Lombardo (1988).

Fig 2. Location of study samples on radar map. Black numbers: andalusite leucogranite with subsolidus sillimanite. UHHC: upper HHC; LHHC: Lower HHC; HHT: High Himalayan Thrust; STDS: South Tibetan Detachment System. Tectonic boundaries from Kali et al. (2010).

Fig 3. Photomicrographs illustrating andalusite and sillimanite textures, symbols of minerals as Kretz (1983). a – sample VS38a: brown fibrolitic sillimanite around a plagioclase enclosing a single andalusite grain without sillimanite border; b – sample VS38b: a grain of andalusite+quartz in a plagioclase core; c – sample V731: single anhedral pink andalusite enclosed in plagioclase; d – sample V328: single andalusite grain replaced by euhedral muscovite in euhedral contact with biotite; e, f – sample V93: clusters of small, randomly oriented andalusite grains enclosed in biotite and (f) a single euhedral andalusite, brown fibrolitic sillimanite fills mineral junction in matrix; g – sample V328b: single andalusite grain with muscovite mantle in matrix, but without muscovite mantle when enclosed in plagioclase; h (b)- sample V927: single andalusite grain with subsolidus muscovite mantle (Na/Na+K = 0.052); i – sample V471: intergranular cluster of randomly oriented subhedral andalusite with muscovite mantle; l – V473: subhedral andalusite replaced by acicular sillimanite; m – sample V472: intergranular cluster of randomly oriented, packed, rounded

andalusite partially enclosed in plagioclase; brown sillimanite grows on clusters only outside plagioclase; n - sample V730: acicular sillimanite growing on biotite.

Fig 4. Compositions of coexisting micas. **(a)** Biotite compositions in phlogopite-annite-eastonite-siderophylite system. **(b)** Molecular (FeO+MnO+MgO) vs. TiO_2. Tie lines join coexisting muscovite and biotite pairs.

Fig 5. A) Cathodoluminescence images of representative zircon grains, with location of laser ablation spot. B) Concordant ages obtained on zircon domains with low CL emission and mean concordia age. All errors given at 2 sigma level.

Fig 6. P-T diagram showing paths during generation and crystallisation of studied leucogranite, as constrained by andalusite and magmatic muscovite stability. Comparison with P-T path proposed for Miocene metamorphism in upper HHC of Makalu area (Pognante and Benna,1993; Streule et al., 2010). 1) metapelite melting, curves for metamorphic and melting reactions in muscovite- and biotite-metapelite from White et al. (2001); 2) hypothetical position of H_2O-saturated Al-saturated boron-rich granite solidus. Al_2SiO_5 phase relations after Pattison (1992) (P92) and Richardson et al.(1969) (R69). Symbols of minerals as Kretz (1983). Grey area: low pressure stability field of magmatic muscovite.

Fig. 7. Sketch (not to scale) of hypothesised interpretative model for generation of andalusite–bearing leucogranite. Higher Himalayan Crystallines tectonic unit is confined between the upper STDS (South Tibetan Detachment System) and the lower MCT (Main Central Thrust). Light grey arrows: represent parabolic particle velocity path in the HHC. Boxes: are rocks located at different structural levels in the tectonic units. Dark grey boxes: are deeper rocks which that move faster upwards towards the surface and at low pressure can transfer heat to upper colder rocks above (light grey box, upper left), giving rise to andalusite-bearing leucogranite. Deeper rocks in the core of HHC (dark grey box, lower right) may have originated leucogranite, owing to decompression melting.

TAB 1. Representative compositions of biotite and muscovite in textural equilibrium. D_{Ti}^{Bt-Ms} range is 1.30-22.07, excluding all values greater than 8.00; mean 4.51±2.3 (n=22): attainment of chemical equilibrium between mica pairs.

TAB 2. Representative compositions of muscovite: A) magmatic; B) in deformed granite. TiO_2 and Na/(Na+K) ratio values are typical of non-igneous mica (Monier et al., 1984).

TAB 3. Cordierite analysis of three samples. Sample V23 is zoned and has high Na_2O content, comparable to that of magmatic cordierite.

TAB 4. Representative compositions of andalusite; contents of transition elements is very low is all grains analysed.

TAB 5. U/Pb isotope ratios of zircon and apparent ages.

TAB 6. Major element compositions and accessory thermometry of two-mica andalusite leucogranite from Everest-Masang Kang area. Data sources: a) Makalu: Palivcova et al. (1982); b) Lagoi Kangri dome: Debon et al., 1986; c) Gophu Ka and Lunana: Castelli and Lombardo (1988); d) Makalu-Kharta area: Visonà and Lombardo (2002); e) Mabja-Kuday dome: Zhang et al. (2004); f) this work.

APPENDIX

Sampled areas. *Makalu.* Palivcova et al. (1982) described the Makalu West Wall as formed of two overlapping units, both consisting of schists and granite and separated by a low-angle, north-dipping thrust. The lower unit mainly contains cataclastic tourmaline granite with cordierite and sillimanite. The upper unit consists of a lower thin injection zone (about 1000 m thick) with schists and highly leucocratic granite (containing tourmaline, cordierite, garnet and sillimanite), and an upper zone (at least 2000 m thick) essentially composed of fine-grained two-mica granite, containing centimetric pods of tourmaline and occasionally sillimanite and andalusite. The upper unit was sampled in 2002 by an Italian mountaineering expedition above the "injection zone" along the path towards Makalu La and the main peak. Between altitudes of 6600 to 7450 m, two-mica granites with sporadic centimetric pods of tourmaline and rare tourmaline granite occur. Samples with andalusite were collected at altitudes of 6650, 7075 and 7400 m (V2-3, V275 and V218, respectively. Fig 2) and, in the latter case, the two-mica granite, was in contact with a small body of tourmaline granite, also containing andalusite.

In the Kama Chu-Phung Chu (Kharta)-Rongbuk area, the sampled dykes cut the garnet-sillimanite *Kharta* gneiss (Borghi et al., 2003) slightly above the hanging wall of the western side of the Ama Drime Massif (sample locations: Fig. 2). Dykes of andalusite-bearing leucogranite (two-mica granite, V953 and foliated tourmaline granite, V927) also occur within the Ama Drime orthogneiss unit (Kali et al., 2010). Sample V916 was collected from debris of andalusite-bearing tourmaline granite from higher parts of the Ama Drime range. Dykes of two-mica andalusite-bearing leucogranite were found in the HHC immediately below the South Tibetan Detachment

near Doya La (VDL), and a foliated and deformed dyke of tourmaline granite (V391) was sampled along the road in the Rongbuk valley.

Kangchenjunga-Sikkim area. In the Zemu valley (about 4500 m), a two-mica granite was sampled (with andalusite, cordierite and brown fibrolite, sample VS14), together with a peculiar two-mica leucogranite containing pink andalusite veinlets, up to 5 mm thick, parallel to the foliation in the rock (sample VS10). Sample VS38 comes from pseudo-concordant sills of two-mica granite (with cordierite, brown fibrolite and xenocrystic sillimanite) cutting the uppermost part of the HHC north of Yume Sandong.

Figure 1

Click here to download high resolution image

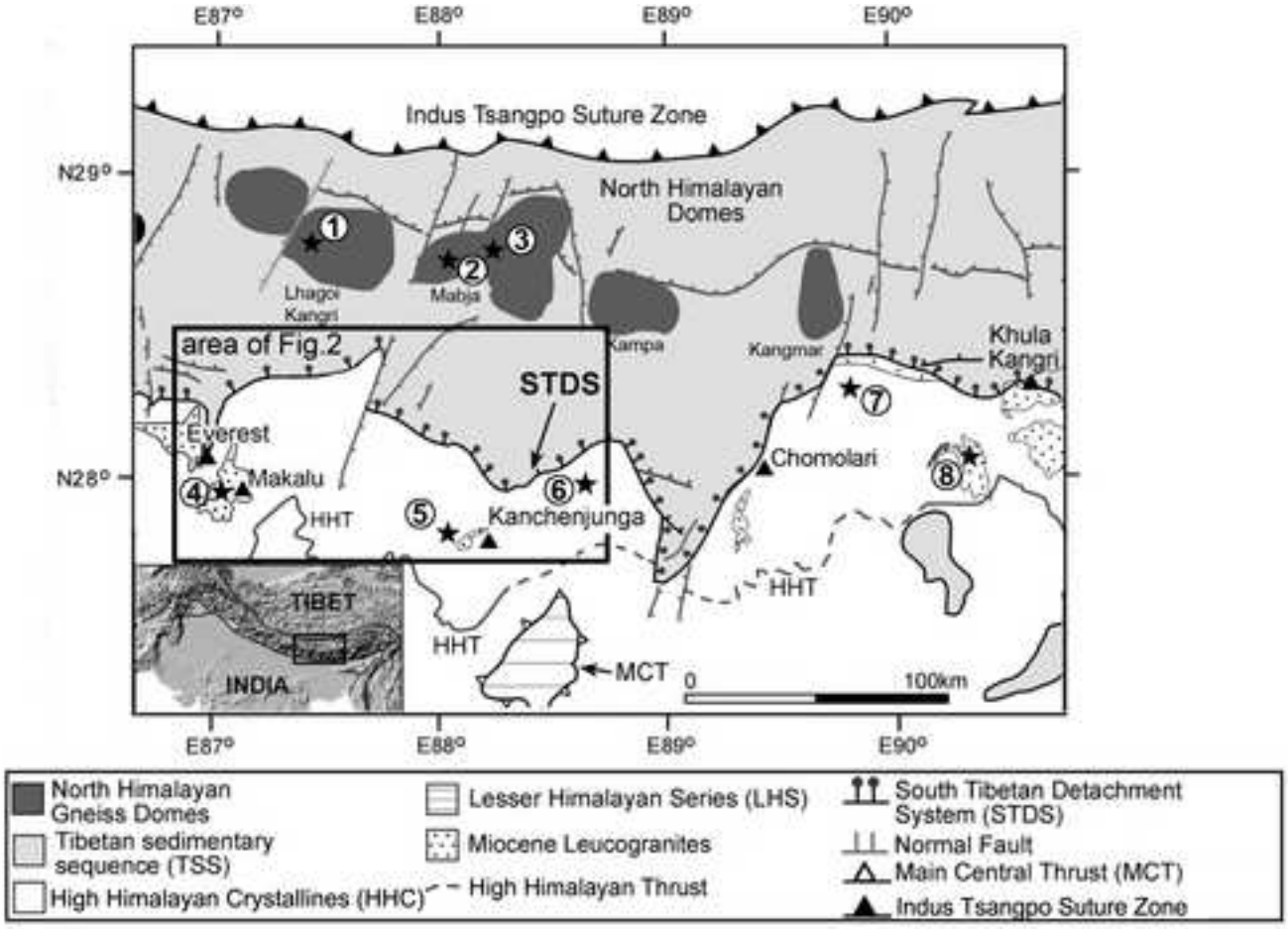

Figure 2

Click here to download high resolution image

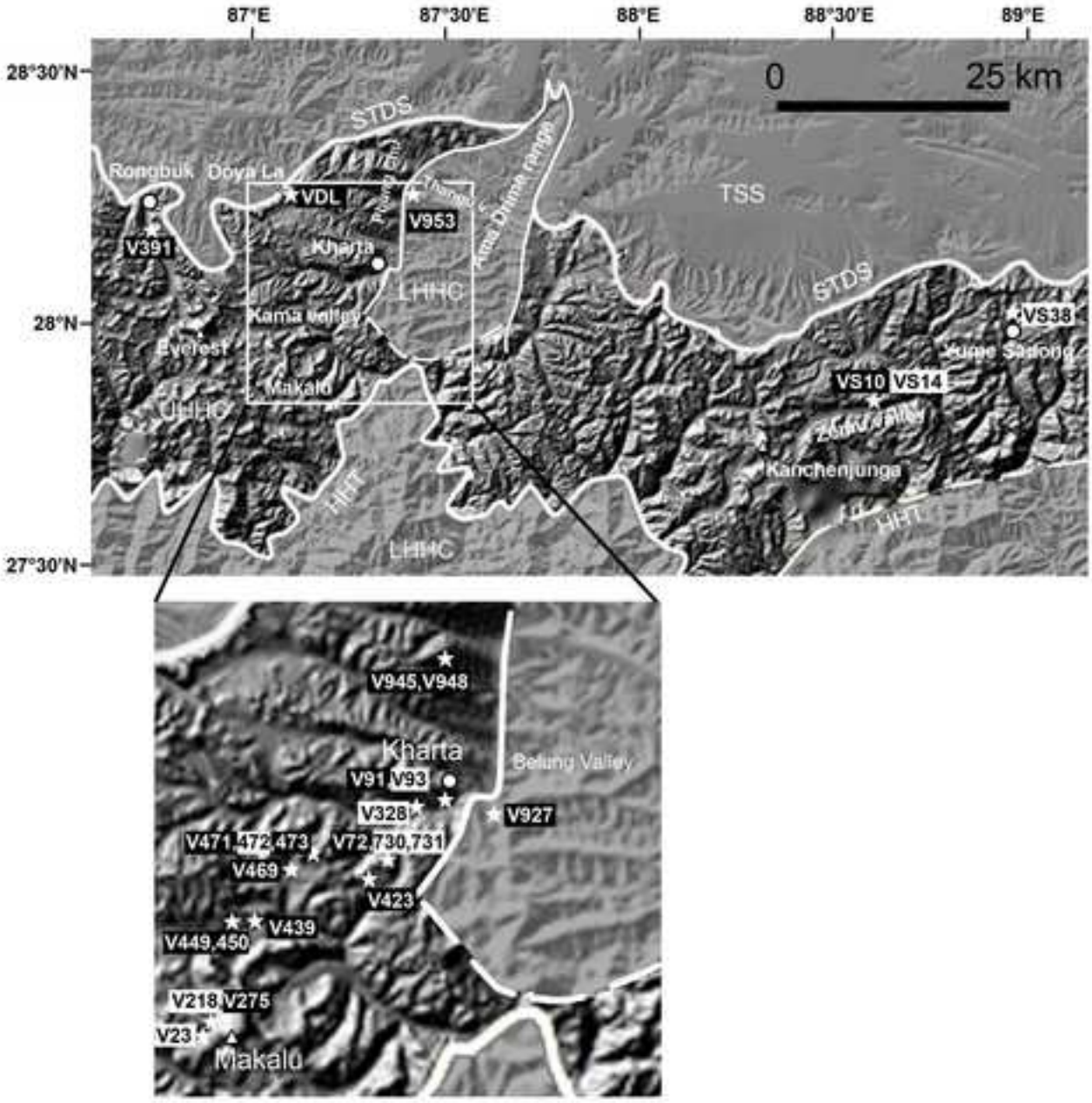

Figure 3

Click here to download high resolution image

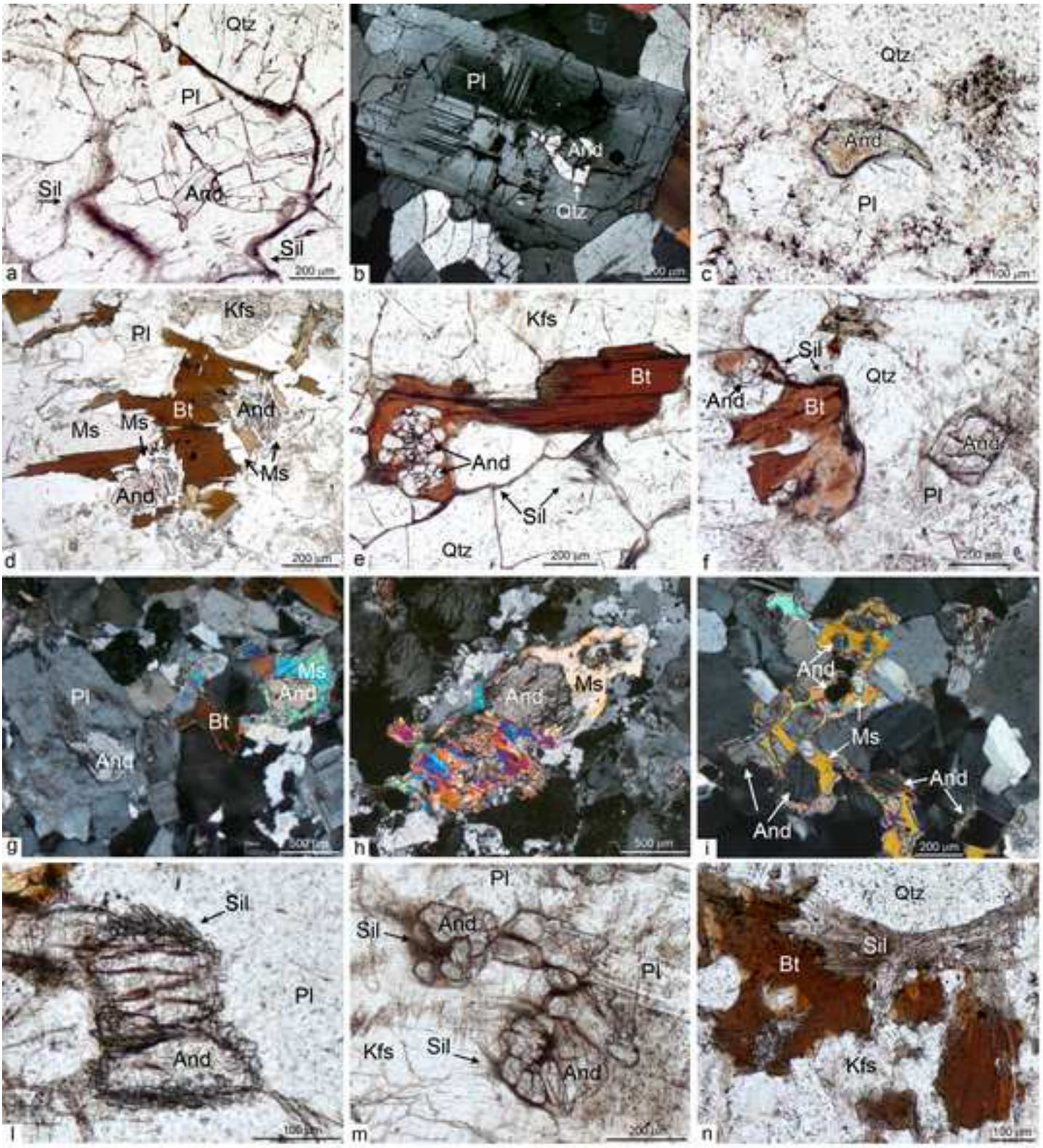

Figure 4

Click here to download high resolution image

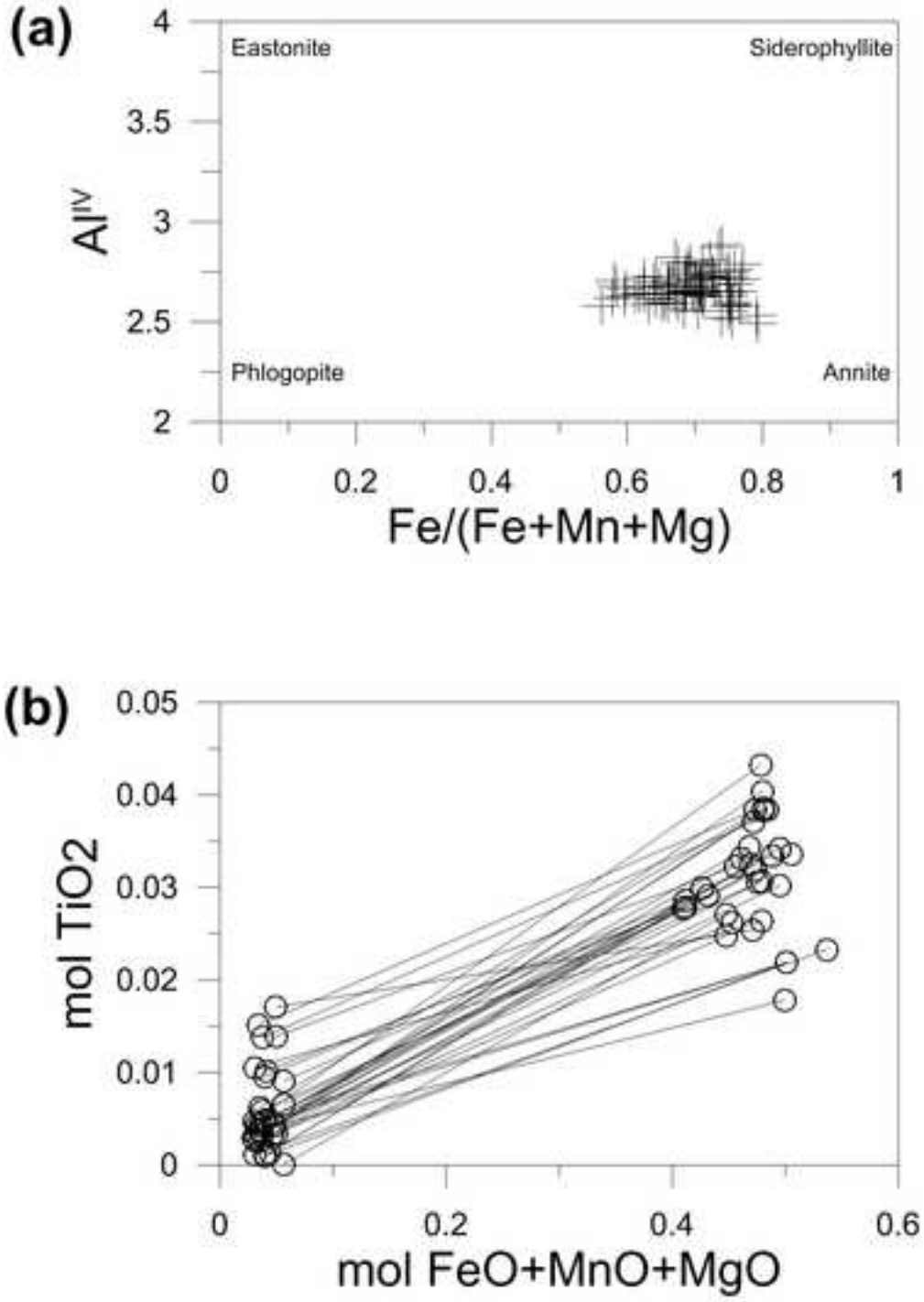

Fig 4

Figure 5

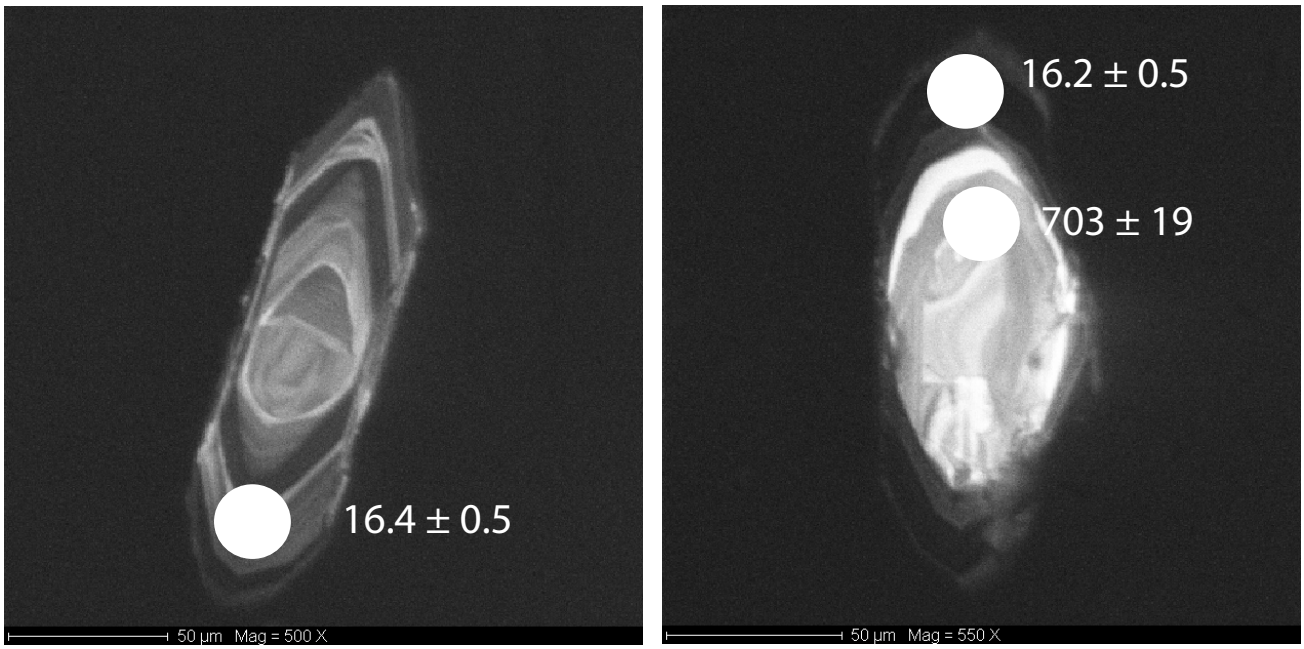
16.4 ± 0.5
50 µm Mag = 500 X
16.2 ± 0.5
703 ± 19
50 µm Mag = 550 X

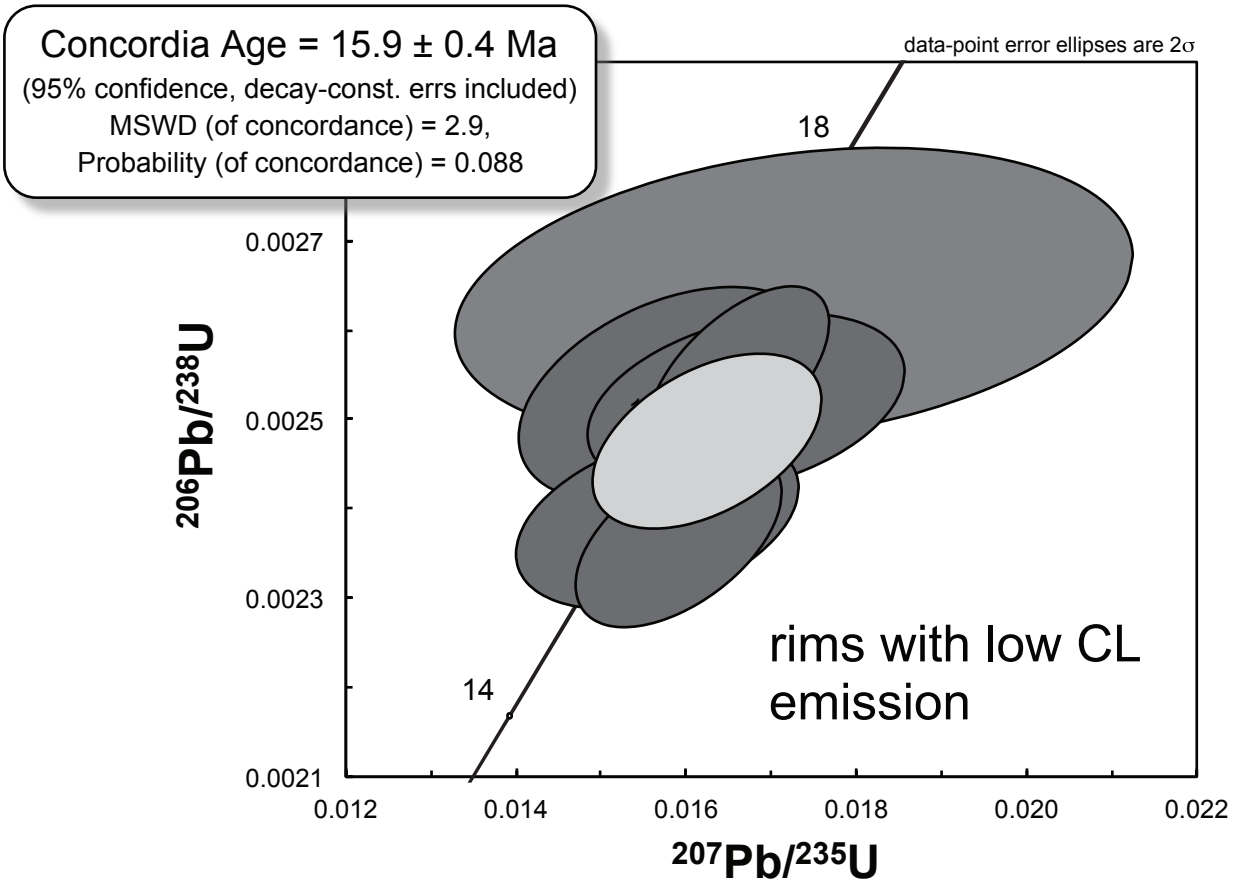
Concordia Age = 15.9 ± 0.4 Ma
(95% confidence, decay-const. errs included)
MSWD (of concordance) = 2.9,
Probability (of concordance) = 0.088
data-point error ellipses are 2σ
18
14
rims with low CL emission
0.0027
0.0025
0.0023
0.0021
0.012
0.014
0.016
0.018
0.020
0.022
206Pb/238U
207Pb/235U

Figure 6

Click here to download high resolution image

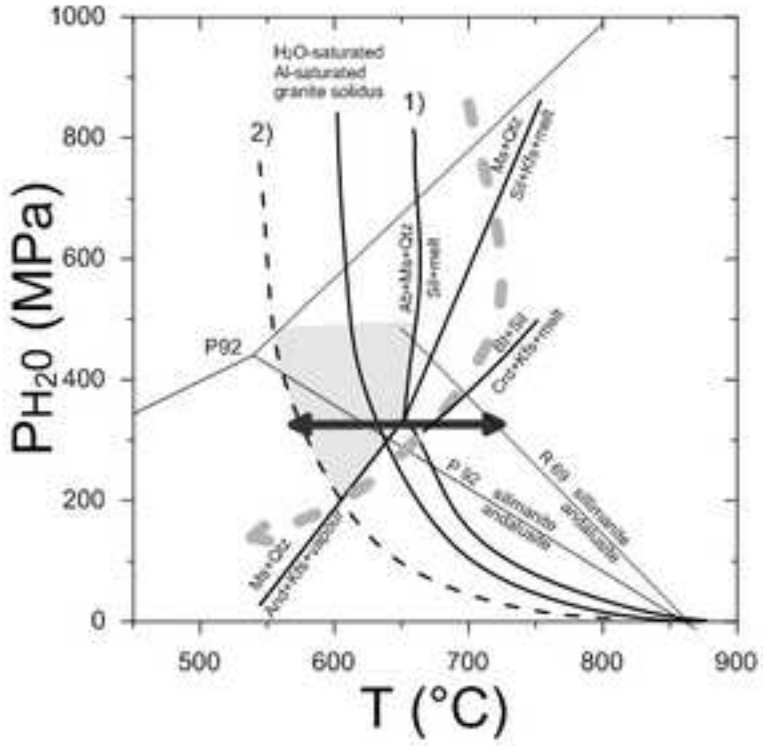

Figure 7

Click here to download high resolution image

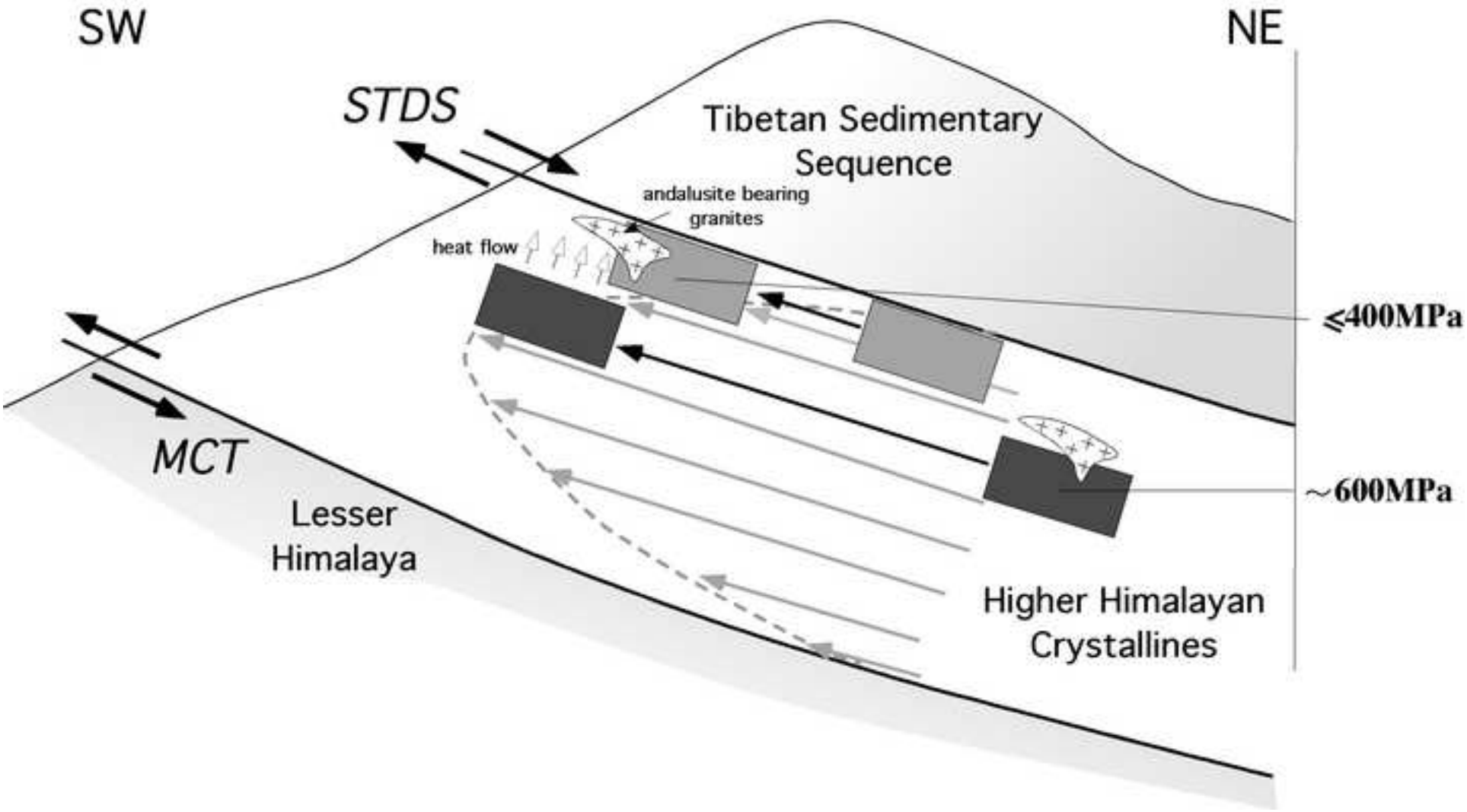

Table 1

Click here to download Table: Table 1.xlsx

Tab 1

	V328		VS38		V449		V945		VS10		V275		V439		V23		V730	
	mu	bt	mu	bt	mu	bt	mu	bt	mu	bt	mu	bt	mu	bt	mu	bt	mu	bt
SiO_2	45.76	35.40	46.37	35.76	45.91	34.79	45.86	34.89	46.45	35.52	45.88	35.98	46.04	34.63	45.91	34.76	45.50	30.62
TiO_2	0.22	1.17	1.32	3.17	0.50	2.91	0.27	1.98	0.84	2.11	0.81	2.23	1.21	3.07	1.11	2.58	0.23	1.86
Al_2O_3	34.18	20.35	34.58	19.55	34.99	19.87	34.68	20.57	35.90	19.81	34.93	20.51	35.17	19.49	34.55	19.59	36.10	21.01
Cr_2O_3	0.04	0.00	0.00	0.01	0.04	0.04	0.00	0.00	0.00	0.02	0.00	0.05	0.00	0.03	0.00	0.00	0.00	0.01
FeO	2.40	21.85	1.19	22.86	1.58	22.86	2.05	24.61	1.26	22.44	1.51	23.46	1.24	24.82	1.76	22.93	1.38	29.21
MnO	0.07	0.56	0.00	0.25	0.05	0.50	0.09	0.57	0.00	0.36	0.00	0.69	0.00	0.39	0.09	0.23	0.00	0.62
MgO	0.92	7.25	0.71	6.03	0.91	4.92	0.81	3.91	0.54	6.52	0.80	3.04	0.67	4.94	0.98	5.37	0.41	4.90
CaO	0.00	0.02	0.00	0.01	0.01	0.00	0.02	0.00	0.03	0.00	0.00	0.01	0.00	0.00	0.02	0.02	0.00	0.05
Na_2O	0.42	0.13	0.54	0.12	0.70	0.00	0.58	0.01	0.68	0.14	0.69	0.00	0.54	0.00	0.59	0.00	0.70	0.03
K_2O	10.58	9.51	10.38	9.36	10.17	9.12	9.86	8.93	10.17	9.05	9.82	9.01	10.49	9.23	10.30	9.36	10.35	5.82
F	0.46	0.76	0.21	1.06	0.56	0.60	0.63	1.18	0.26	0.48	1.11	1.09	0.11	0.45	0.79	1.98	0.12	0.00
Total	95.04	96.98	95.30	98.19	95.42	95.60	94.84	96.66	96.13	96.44	95.57	96.07	95.46	97.03	96.10	96.82	94.79	94.12
O=F,Cl	-0.19	-0.32	-0.09	-0.45	-0.24	-0.25	-0.26	-0.50	-0.11	-0.20	-0.47	-0.46	-0.05	-0.19	-0.33	-0.83	-0.05	0.00
Total	94.85	96.66	95.21	97.75	95.18	95.35	94.58	96.16	96.02	96.24	95.10	95.61	95.42	96.84	95.77	95.98	94.74	94.12
Numbers of ions on the basis of 23 O																		
Si	6.153	5.353	6.168	5.354	6.112	5.361	6.141	5.345	6.116	5.400	6.085	5.503	6.120	5.313	6.085	5.291	6.088	4.908
Al^{IV}	1.847	2.647	1.832	2.646	1.888	2.639	1.859	2.655	1.884	2.600	1.915	2.497	1.880	2.687	1.915	2.709	1.912	3.092
Al^{VI}	3.569	0.979	3.589	0.802	3.602	0.969	3.614	1.060	3.688	0.949	3.544	1.200	3.631	0.836	3.482	0.806	3.782	0.877
Ti	0.022	0.133	0.132	0.357	0.050	0.337	0.027	0.228	0.084	0.241	0.081	0.256	0.121	0.354	0.111	0.295	0.023	0.225
Cr	0.004	0.000	0.000	0.001	0.004	0.005	0.000	0.000	0.000	0.003	0.000	0.006	0.000	0.003	0.000	0.000	0.000	0.002
Fe^{2+}	0.270	2.763	0.132	2.862	0.176	2.947	0.230	3.154	0.138	2.854	0.168	3.000	0.138	3.184	0.195	2.919	0.155	3.916
Mn	0.008	0.072	0.000	0.032	0.006	0.065	0.011	0.074	0.000	0.046	0.000	0.089	0.000	0.051	0.010	0.030	0.000	0.084
Mg	0.184	1.634	0.141	1.346	0.180	1.129	0.161	0.894	0.107	1.477	0.159	0.694	0.133	1.130	0.193	1.219	0.081	1.171
Sito O	4.057	5.580	3.994	5.400	4.018	5.453	4.043	5.409	4.017	5.569	3.952	5.246	4.022	5.559	3.991	5.269	4.041	6.274
Ca	0.000	0.003	0.000	0.002	0.002	0.000	0.002	0.000	0.004	0.000	0.001	0.001	0.000	0.000	0.002	0.003	0.000	0.009
Na	0.119	0.038	0.139	0.034	0.180	0.000	0.151	0.003	0.173	0.040	0.178	0.000	0.139	0.000	0.150	0.000	0.183	0.008
K	1.814	1.835	1.762	1.788	1.727	1.792	1.685	1.746	1.708	1.755	1.662	1.757	1.779	1.806	1.742	1.818	1.767	1.190
Sito A	1.922	1.876	1.901	1.824	1.908	1.792	1.839	1.749	1.885	1.795	1.841	1.758	1.917	1.806	1.894	1.821	1.950	1.207
F	0.194	0.363	0.090	0.504	0.236	0.291	0.265	0.573	0.107	0.232	0.464	0.527	0.046	0.217	0.331	0.951	0.051	0.000
Total	14.17	15.82	13.98	15.73	14.16	15.54	14.15	15.73	14.01	15.60	14.26	15.53	13.99	15.58	14.22	16.04	14.04	15.48
O=F,Cl	-0.19	-0.36	-0.09	-0.50	-0.24	-0.29	-0.26	-0.57	-0.11	-0.23	-0.46	-0.53	-0.05	-0.22	-0.33	-0.95	-0.05	0.00
Total	13.98	15.46	13.90	15.22	13.93	15.25	13.88	15.16	13.90	15.36	13.79	15.00	13.94	15.36	13.89	15.09	13.99	15.48
AlTot	5.416	3.626	5.421	3.448	5.490	3.608	5.473	3.714	5.572	3.549	5.459	3.697	5.511	3.524	5.397	3.515	5.693	3.969
Na/(Na+K)	0.061	0.020	0.073	0.018	0.094	0.000	0.082	0.002	0.092	0.022	0.097	0.000	0.072	0.000	0.080	0.000	0.094	0.007
$D_{Ti}^{Bt/Ms}$	5.355		2.408		1.309		7.413		2.498		2.745		2.537		2.320		7.995	

Table 2

Click here to download Table: Table 2.xlsx

Tab 2

A) magmatic muscovite replacing andalusite

	VS10				VM3		V439		V730	
	SK10E1	SK10E1	SK10E1	10B12	3-1A4	3-1A5	39a8	39a9	30B2	30B4
SiO_2	46.39	45.68	46.95	46.32	46.78	48.57	46.38	46.30	46.35	46.08
TiO_2	0.05	0.00	0.30	0.00	0.34	0.00	0.03	0.24	0.06	0.07
Al_2O_3	37.81	38.77	36.08	36.95	35.50	33.74	36.45	35.76	36.68	36.36
Cr_2O_3	0.00	0.00	0.00	0.00	0.00	0.01	0.04	0.00	0.00	0.01
FeO	0.33	0.26	1.05	0.82	1.77	1.19	1.36	1.46	1.12	1.51
MnO	0.03	0.00	0.04	0.00	0.00	0.03	0.01	0.00	0.03	0.01
MgO	0.04	0.00	0.55	0.30	0.96	0.52	0.46	0.69	0.34	0.34
CaO	0.00	0.00	0.00	0.03	0.00	0.00	0.00	0.02	0.00	0.00
Na_2O	0.78	0.73	0.81	0.53	0.75	0.47	0.76	0.56	0.71	0.59
K_2O	9.94	10.13	9.93	10.29	10.11	10.12	10.16	10.17	10.53	10.09
F	0.14	0.00	0.60	0.50	0.68	0.04	0.37	0.27	0.35	0.11
Total	95.51	95.57	96.31	95.73	96.89	94.68	96.04	95.47	96.16	95.15
O=F,Cl	-0.06	0.00	-0.25	-0.21	-0.29	-0.02	-0.16	-0.11	-0.15	-0.04
Total	95.45	95.57	96.06	95.52	96.61	94.66	95.88	95.35	96.02	95.11
Numbers of ions on the basis of 23 O										
Si	6.098	6.008	6.150	6.102	6.126	6.454	6.112	6.140	6.104	6.125
Al^{IV}	1.902	1.992	1.850	1.898	1.874	1.546	1.888	1.860	1.896	1.875
Al^{VI}	3.955	4.016	3.721	3.840	3.606	3.738	3.773	3.729	3.797	3.821
Ti	0.005	0.000	0.030	0.000	0.034	0.000	0.003	0.024	0.006	0.007
Cr	0.000	0.000	0.000	0.000	0.000	0.001	0.004	0.000	0.000	0.001
Fe^{2+}	0.036	0.029	0.115	0.090	0.193	0.132	0.150	0.162	0.123	0.167
Mn	0.003	0.000	0.004	0.000	0.000	0.003	0.001	0.000	0.003	0.001
Mg	0.009	0.000	0.107	0.060	0.187	0.103	0.090	0.136	0.067	0.067
Sito O	4.008	4.045	3.977	3.990	4.020	3.977	4.021	4.051	3.996	4.065
Ca	0.000	0.000	0.000	0.004	0.000	0.000	0.001	0.003	0.000	0.000
Na	0.199	0.185	0.206	0.134	0.190	0.121	0.195	0.145	0.182	0.152
K	1.668	1.700	1.660	1.730	1.690	1.715	1.708	1.720	1.769	1.711
Sito A	1.866	1.885	1.866	1.868	1.879	1.837	1.904	1.868	1.951	1.863
F	0.056	0.000	0.250	0.207	0.281	0.017	0.156	0.113	0.145	0.045
Total	13.930	13.931	14.092	14.065	14.180	13.830	14.082	14.031	14.092	13.973
O=F,Cl	-0.056	0.000	-0.250	-0.207	-0.281	-0.017	-0.156	-0.113	-0.145	-0.045
Total	13.874	13.931	13.842	13.858	13.899	13.813	13.926	13.918	13.947	13.928
AlTot	5.857	6.009	5.570	5.738	5.479	5.284	5.661	5.589	5.693	5.696
Na/(Na+K)	0.106	0.098	0.110	0.072	0.101	0.066	0.103	0.078	0.093	0.082

B) muscovite in deformed granites

	replacing andalusite						with sillimanite		
	V953			V927			V218		
SiO_2	45.78	46.77	46.34	45.66	44.17	44.95	42.38	42.22	42.88
TiO_2	0.03	0.05	0.03	0.03	0.00	0.06	0.01	0.02	0.00
Al_2O_3	36.27	37.13	36.34	37.16	37.10	36.21	33.29	27.28	31.54
Cr_2O_3	0.01	0.03	0.01	0.00	0.01	0.05	0.00	0.04	0.00
FeO	1.18	0.85	1.17	1.43	0.79	1.29	4.58	9.02	5.76
MnO	0.00	0.00	0.04	0.00	0.05	0.04	0.02	0.10	0.15
MgO	0.53	0.60	0.70	0.15	0.06	0.13	2.49	6.88	4.29
CaO	0.01	0.01	0.00	0.02	0.00	0.00	0.03	0.01	0.00
Na_2O	0.43	0.42	0.39	0.37	0.40	0.36	0.36	0.22	0.25
K_2O	10.83	10.75	10.69	10.45	10.58	10.33	10.16	10.05	10.48
F	0.42	0.00	0.38	0.00	0.00	0.36	0.00	0.14	0.39
Total	95.51	96.61	96.08	95.27	93.14	93.78	93.33	95.99	95.75
O=F,Cl	-0.18	0.00	-0.16	0.00	0.00	-0.15	0.00	-0.06	-0.17
Total	95.33	96.61	95.92	95.26	93.14	93.63	93.33	95.93	95.58
Numbers of ions on the basis of 23 O									
Si	6.084	6.119	6.111	6.069	6.004	6.071	5.899	5.897	5.881
Al^{IV}	1.916	1.881	1.889	1.931	1.996	1.929	2.101	2.103	2.119
Al^{VI}	3.766	3.843	3.759	3.889	3.947	3.836	3.361	2.388	2.979
Ti	0.003	0.005	0.003	0.003	0.000	0.006	0.001	0.002	0.000
Cr	0.001	0.003	0.001	0.000	0.001	0.005	0.000	0.005	0.000
Fe^{2+}	0.131	0.093	0.129	0.159	0.090	0.146	0.533	1.054	0.660
Mn	0.000	0.000	0.004	0.000	0.005	0.005	0.003	0.012	0.018
Mg	0.105	0.117	0.138	0.029	0.012	0.027	0.516	1.433	0.877
Sito O	4.007	4.060	4.034	4.081	4.054	4.024	4.413	4.895	4.534
Ca	0.002	0.002	0.000	0.003	0.000	0.000	0.004	0.001	0.000
Na	0.111	0.108	0.099	0.095	0.105	0.095	0.098	0.060	0.068
K	1.837	1.794	1.798	1.773	1.834	1.779	1.804	1.791	1.833
Sito A	1.950	1.904	1.897	1.870	1.940	1.874	1.907	1.852	1.901
F	0.175	0.000	0.157	0.000	0.000	0.153	0.000	0.063	0.170
Total	14.13	13.96	14.09	13.95	13.99	13.90	14.32	14.75	14.44
O=F,Cl	-0.18	0.00	-0.16	0.00	0.00	-0.15	0.00	-0.06	-0.17
Total	13.96	13.96	13.93	13.95	13.99	14.05	14.32	14.81	14.61
AlTot	5.682	5.724	5.648	5.821	5.944	5.765	5.462	4.492	5.098
Na/(Na+K)	0.057	0.057	0.052	0.051	0.054	0.051	0.052	0.032	0.036

Table 3

Click here to download Table: Table 3.xlsx

Tab 3

	V93		V275	V328*	V423		V439*		V927*	V948*	V449	V953	VS10*			VS38		VM3*		
	core	rim			core	rim	core*	rim					core*	int*	rim*	core	core	core*	core*	rim*
SiO2	36.49	36.41	36.90	36.47	35.96	36.74	36.93	36.89	36.51	36.53	36.47	36.39	36.88	36.60	36.69	37.34	37.07	36.77	37.13	36.69
TiO2	0.03	0.03	0.01	0.02	0.02	0.11	0.06	0.08	0.03	0.06	0.05	0.05	0.11	0.06	0.08	0.04	0.06	0.09	0.01	0.01
Al2O3	63.35	63.55	63.30	62.75	64.29	63.65	64.15	63.61	63.33	64.03	63.63	63.96	63.85	63.72	63.00	63.25	63.22	63.88	63.63	63.93
FeO	0.47	0.35	0.36	0.41	0.48	0.63	0.40	0.71	0.58	0.34	0.24	0.37	0.46	0.56	0.51	0.51	0.43	0.39	0.36	0.30
MnO	0.00	0.00	0.01	0.02	0.02	0.00	0.00	0.01	0.00	0.04	0.01	0.00	0.00	0.01	0.00	0.00	0.00	0.00	0.00	0.03
MgO	0.00	0.00	0.04	0.00	0.04	0.01	0.01	0.02	0.00	0.02	0.01	0.01	0.06	0.07	0.00	0.06	0.03	0.07	0.00	0.00
CaO	0.01	0.00	0.00	0.00	0.01	0.02	0.02	0.00	0.00	0.00	0.00	0.00	0.03	0.02	0.01	0.02	0.00	0.00	0.00	0.01
Na2O	0.00	0.00	0.00	0.00	0.05	0.00	0.00	0.01	0.00	0.00	0.00	0.00	0.05	0.00	0.03	0.00	0.00	0.00	0.00	0.00
K2O	0.00	0.00	0.02	0.02	0.02	0.02	0.01	0.00	0.00	0.01	0.00	0.01	0.00	0.01	0.00	0.01	0.01	0.00	0.00	0.00
Total	100.34	100.34	100.65	99.67	100.90	101.17	101.58	101.32	100.45	101.02	100.41	100.78	101.43	101.04	100.32	101.23	100.83	101.20	101.13	100.97
Numbers of ions on the basis of 20 O																				
Si	3.932	3.923	3.962	3.955	3.859	3.931	3.931	3.941	3.932	3.911	3.925	3.905	3.934	3.920	3.955	3.987	3.974	3.929	3.967	3.928
Ti	0.002	0.003	0.001	0.002	0.001	0.008	0.005	0.006	0.002	0.004	0.004	0.004	0.009	0.005	0.006	0.003	0.005	0.007	0.001	0.001
Al	8.049	8.071	8.014	8.023	8.136	8.027	8.050	8.011	8.041	8.081	8.073	8.091	8.028	8.046	8.007	7.964	7.990	8.047	8.014	8.068
Fe^{2+}	0.038	0.028	0.029	0.033	0.039	0.051	0.032	0.057	0.047	0.028	0.020	0.030	0.037	0.045	0.041	0.041	0.035	0.031	0.029	0.024
Mn	0.000	0.000	0.001	0.001	0.002	0.000	0.000	0.001	0.000	0.003	0.001	0.000	0.000	0.001	0.000	0.000	0.000	0.000	0.000	0.003
Mg	0.000	0.000	0.006	0.000	0.006	0.001	0.002	0.004	0.000	0.002	0.001	0.001	0.010	0.010	0.000	0.009	0.005	0.011	0.000	0.000
Ca	0.001	0.000	0.000	0.000	0.002	0.002	0.002	0.000	0.000	0.000	0.000	0.000	0.003	0.002	0.001	0.002	0.000	0.000	0.000	0.002
Na	0.000	0.000	0.000	0.000	0.011	0.000	0.000	0.001	0.000	0.000	0.000	0.000	0.010	0.000	0.006	0.000	0.000	0.000	0.000	0.000
K	0.000	0.000	0.003	0.002	0.003	0.002	0.001	0.000	0.000	0.001	0.000	0.001	0.000	0.001	0.000	0.001	0.001	0.000	0.000	0.000
Total	12.02	12.02	12.02	12.02	12.06	12.02	12.02	12.02	12.02	12.03	12.02	12.03	12.03	12.03	12.02	12.01	12.01	12.03	12.01	12.03

* pink grains or zone of grains

Table 4

Click here to download Table: Table 4.xlsx

Tab 4

	V23						V472				V93		
wt%	core	core	int.	int.	int.	rim	core	core	int.	rim	core	int.	rim
SiO_2	47.20	48.06	47.60	48.05	47.91	47.89	47.60	47.40	48.11	46.92	47.68	47.53	47.48
TiO_2	bdl	bdl	bdl	bdl	bdl	bdl	bdl	0.02	bdl	bdl	0.01	bdl	0.01
Al_2O_3	31.17	31.57	31.92	31.51	31.88	31.75	31.98	31.94	31.97	31.00	31.66	32.14	31.84
FeO	11.52	11.51	11.05	11.17	11.04	11.18	10.89	12.41	9.41	13.53	12.89	12.86	12.81
MnO	0.39	0.38	0.40	0.37	0.39	0.32	0.43	0.65	0.37	0.90	0.43	0.42	0.54
MgO	4.94	5.08	5.10	5.21	5.11	4.96	6.28	5.18	7.12	4.29	5.22	5.21	5.14
CaO	bdl	bdl	0.05	0.04	0.03	0.03	0.03	bdl	0.02	0.01	0.01	0.02	0.03
Na_2O	1.59	1.55	1.35	1.20	1.20	1.00	0.49	0.57	0.47	0.61	0.63	0.56	0.63
K_2O	0.01	bdl	0.01	0.03	0.01	0.02	bdl	0.01	bdl	0.02	bdl	0.02	bdl
Total	96.83	98.17	97.47	97.58	98.01	97.14	97.71	98.17	97.48	97.31	98.52	99.03	98.49
Numbers of ions on the basis of 18 O													
Si	5.044	5.058	5.034	5.073	5.054	5.072	5.008	5.004	5.034	5.034	5.022	4.993	5.005
Ti	0.000	0.000	0.000	0.000	0.000	0.000	0.000	0.002	0.000	0.000	0.000	0.000	0.001
Al^{IV}	3.928	3.916	3.981	3.923	3.966	3.964	3.966	3.975	3.943	3.922	3.931	3.981	3.958
Sum T	8.972	8.974	9.015	8.996	9.019	9.037	8.973	8.978	8.977	8.956	8.953	8.974	8.962
AlVI	0.000	0.000	0.010	0.000	0.019	0.037	0.000	0.000	0.000	0.000	0.000	0.000	0.000
Fe	1.030	1.013	0.978	0.987	0.974	0.990	0.958	1.096	0.824	1.214	1.136	1.130	1.130
Mn	0.035	0.034	0.036	0.033	0.035	0.028	0.039	0.059	0.033	0.081	0.038	0.038	0.048
Mg	0.788	0.797	0.803	0.820	0.803	0.783	0.984	0.814	1.111	0.687	0.819	0.815	0.807
Sum B	1.852	1.844	1.816	1.840	1.832	1.838	1.981	1.969	1.967	1.982	1.993	1.982	1.985
Ca	0.000	0.000	0.005	0.004	0.004	0.003	0.003	0.000	0.002	0.002	0.001	0.002	0.003
Na	0.329	0.317	0.277	0.247	0.245	0.205	0.100	0.116	0.096	0.128	0.128	0.114	0.130
K	0.001		0.001	0.004	0.002	0.002	0.000	0.002	0.000	0.002	0.000	0.002	0.000
Sum A	0.331	0.317	0.284	0.255	0.251	0.210	0.103	0.118	0.098	0.132	0.129	0.118	0.133
Total	11.155	11.135	11.115	11.091	11.086	11.049	11.058	11.067	11.042	11.070	11.076	11.075	11.081
Fe/(Fe+Mg)	0.57	0.56	0.55	0.55	0.55	0.56	0.49	0.57	0.43	0.64	0.58	0.58	0.58

bdl below detection limit

Table 5

Click here to download Table: TAB 5.pdf

		Isotope Ratios						Apaprent ages					
Run name	Grain/position	Pb207/Pb206	1s	Pb206/U238	1s	Pb207/U235	1s	Pb206/U238	1s	Pb207/U235	1s	Concordia age	2s
Fe23a004	Z1 rim	0,0451	0,0021	0,0025	0,0000	0,0158	0,0007	16	0,3	16	0,7	16	0,6
Fe23a005	Z2 core	0,0720	0,0013	0,1600	0,0025	1,5883	0,0307	957	15	966	19	965	24
Fe23a006	Z3 rim	0,0688	0,0012	0,1441	0,0023	1,3663	0,0269	868	14	875	17	873	23
Fe23a007	Z5 rim	0,0773	0,0037	0,0026	0,0001	0,0272	0,0013	16	0,4	27	1,3	---	---
Fe23a008	Z7 rim	0,0479	0,0022	0,0025	0,0000	0,0167	0,0008	16	0,3	17	0,8	16	0,5
Fe23a009	Z7 core	0,0631	0,0013	0,1152	0,0017	1,0012	0,0218	703	11	704	15	703	19
Fe23a010	Z8 core	0,0997	0,0019	0,2833	0,0044	3,8946	0,0792	1608	25	1613	33	1613	33
Fe23a011	Z10 core	0,0684	0,0012	0,1435	0,0022	1,3532	0,0259	865	13	869	17	868	22
Fe23a012	Z11 core	0,0943	0,0018	0,2616	0,0041	3,4000	0,0689	1498	23	1504	30	1504	32
Fe23a013	Z14 rim	0,0663	0,0013	0,1320	0,0021	1,2068	0,0249	799	13	804	17	802	22
Fe23a014	Z14 rim dark	0,0468	0,0021	0,0024	0,0000	0,0156	0,0007	15	0,3	16	0,7	15	0,5
Fe23a015	Z16 rim dark	0,0514	0,0014	0,0026	0,0000	0,0184	0,0005	17	0,3	19	0,5	---	---
Fe23a016	Z17 rim	0,0564	0,0011	0,0712	0,0011	0,5536	0,0114	444	6,9	447	9,2	445	13
Fe23a017	Z18 rim dark	0,0691	0,0037	0,0028	0,0001	0,0261	0,0014	18	0,4	26	1,4	---	---
Fe23a018	Z18 core	0,0669	0,0012	0,1340	0,0020	1,2354	0,0237	811	12	817	16	814	21
Fe23a019	Z24 rim dark	0,0765	0,0091	0,0028	0,0001	0,0294	0,0034	18	0,5	29	3,4	---	---
Fe23a020	Z24 core	0,0579	0,0018	0,0857	0,0014	0,6840	0,0210	530	8,4	529	16	530	16
Fe23a021	Z26 core dark	0,0474	0,0046	0,0026	0,0001	0,0173	0,0016	17	0,4	17	1,7	17	0,9
Fe23a022	Z28 rim dark	0,0584	0,0012	0,0026	0,0000	0,0212	0,0005	17	0,3	21	0,5	---	---
Fe23a023	Z28 core	0,0809	0,0015	0,1417	0,0022	1,5792	0,0316	854	13	962	19	---	---
Fe23a027	Z30 rim dark	0,0533	0,0015	0,0024	0,0000	0,0172	0,0005	15	0,3	17	0,5	---	---
Fe23a028	Z30 core	0,0556	0,0019	0,0735	0,0012	0,5652	0,0191	457	7,5	455	15	457	14
Fe23a029	Z35 rim dark	0,0714	0,0022	0,0025	0,0000	0,0247	0,0008	16	0,3	25	0,8	---	---
Fe23a030	Z35 core	0,0560	0,0012	0,0679	0,0010	0,5244	0,0114	423	6,4	428	9,3	424	12
Fe23a031	Z37 rim dark	0,0706	0,0017	0,0025	0,0000	0,0244	0,0006	16	0,3	25	0,6	---	---

Fe23a032	Z37 core	0,0721	0,0014	0,1626	0,0025	1,6148	0,0332	971	15	976	20	974	25
Fe23a033	Z39 rim dark	0,0631	0,0031	0,0027	0,0000	0,0235	0,0011	17	0,3	24	1,1	---	---
Fe23a034	Z41 core dark	0,0487	0,0015	0,0024	0,0000	0,0159	0,0005	15	0,3	16	0,5	15	0,5
Fe23a035	Z45 rim dark	0,0698	0,0017	0,0025	0,0000	0,0241	0,0006	16	0,3	24	0,6	---	---
Fe23a036	Z45 core	0,0549	0,0014	0,0659	0,0011	0,4986	0,0136	411	6,8	411	11	411	13
Fe23a037	Z47 rim	0,0548	0,0016	0,0598	0,0010	0,4496	0,0138	375	6,4	377	12	375	12
Fe23a038	Z49 rim	0,0557	0,0010	0,0707	0,0011	0,5417	0,0112	440	7,0	440	9,1	440	13
Fe23a039	Z50 rim dark	0,0472	0,0012	0,0026	0,0000	0,0166	0,0004	16	0,3	17	0,4	16	0,5
Fe23a040	Z55 rim dark	0,0616	0,0015	0,0025	0,0000	0,0213	0,0005	16	0,3	21	0,5	---	---
Fe23a041	Z55 core	0,0752	0,0013	0,1529	0,0023	1,5857	0,0305	917	14	965	19		
Fe23a042	Z57 core	0,0663	0,0015	0,1288	0,0020	1,1764	0,0273	781	12	790	18	784	11
Fe23a026	Reference zircon 02123	0,0524	0,0014	0,0477	0,0007	0,3442	0,0095	300	5	300	8	300	9,1
Standards													
Fe23a001	Plesovice STD	0,0536	0,0010	0,0538	0,0008	0,3975	0,0082	---	---	---	---	---	---
Fe23a002	Plesovice STD	0,0523	0,0010	0,0535	0,0008	0,3859	0,0079	---	---	---	---	---	---
Fe23a003	Plesovice STD	0,0540	0,0010	0,0538	0,0008	0,4004	0,0082	---	---	---	---	---	---
Fe23a024	Plesovice STD	0,0536	0,0010	0,0527	0,0008	0,3891	0,0081	---	---	---	---	---	---
Fe23a025	Plesovice STD	0,0529	0,0010	0,0546	0,0008	0,3984	0,0082	---	---	---	---	---	---
Fe23a043	Plesovice STD	0,0523	0,0010	0,0538	0,0008	0,3882	0,0080	---	---	---	---	---	---
Fe23a044	Plesovice STD	0,0542	0,0011	0,0535	0,0008	0,4000	0,0083	---	---	---	---	---	---
Fe23a045	Plesovice STD	0,0541	0,0011	0,0522	0,0008	0,3896	0,0081	---	---	---	---	---	---

Table 6

Click here to download Table: Table 6.xlsx

	a)	b)	c)				d)								e)	f)				
sample	36	XR316	BH14	BH18	BH24	BH10	M3	328B	439	449	450	469	472	473	T117	V471	V91	VS10	VS14	VS38
SiO_2	72.63	72.40	73.12	73.32	73.67	71.79	71.30	72.65	72.63	73.12	72.23	71.49	72.36	72.72	73.85	76.53	75.37	75.58	74.08	72.67
TiO_2	0.15	0.31	0.13	0.13	0.13	0.20	0.17	0.15	0.20	0.18	0.20	0.23	0.23	0.22	0.10	0.04	0.038	0.04	0.11	0.18
Al_2O_3	14.88	14.81	14.87	14.92	14.86	15.78	15.51	14.68	14.74	14.85	14.96	14.80	14.64	14.89	14.81	14.06	14.13	13.66	14.68	14.91
Fe_2O_3	0.89	2.34	0.92	0.93	0.87	1.57	1.68	1.47	1.71	1.49	1.55	1.79	1.77	1.79	1.18	0.58	0.66	0.40	1.17	1.58
MnO	0.02	0.05	0.02	0.01	0.02	0.04	0.03	0.02	0.02	0.02	0.01	0.02	0.02	0.01	0.03	0.01	0.015	0.01	0.03	0.03
MgO	0.78	0.57	0.01	0.08	0.02	0.08	0.34	0.30	0.36	0.33	0.36	0.38	0.38	0.42	0.35	0.12	0.11	0.08	0.19	0.38
CaO	0.88	1.16	0.66	0.66	0.63	0.68	1.03	0.83	0.95	0.78	0.98	0.83	1.02	1.12	0.94	0.51	0.83	0.57	0.83	1.23
Na_2O	3.68	3.74	3.91	4.10	4.04	3.59	4.00	3.34	3.59	3.72	3.73	3.72	3.64	3.54	3.34	3.89	3.3	2.99	3.04	3.45
K_2O	4.91	4.08	4.97	4.82	4.76	5.20	4.89	5.42	4.86	4.55	4.57	4.53	4.49	4.58	4.36	3.32	4.62	5.91	4.86	4.37
P_2O_5	0.12	0.04	0.09	0.14	0.10	0.07	0.14	0.12	0.14	0.16	0.13	0.13	0.11	0.09	0.19	0.15	0.1	0.14	0.10	0.14
LOI	0.70	0.62	1.43	0.98	1.01	0.89	0.76	0.81	0.83	0.91	0.79	1.78	0.73	0.84	0.80	0.69	0.83	0.50	0.80	0.90
Total	99.64	100.13	100.14	100.10	100.12	99.90	99.86	99.80	100.04	100.12	99.52	99.71	99.40	100.23	99.95	99.91	100.01	99.88	99.89	99.84
ASI	1.15	1.17	1.14	1.13	1.15	1.24	1.13	1.14	1.14	1.19	1.16	1.18	1.15	1.16	1.24	1.29	1.18	1.11	1.25	1.18
Q	35	39	33	33	34	34	28	34	36	37	36	36	37	37	41	44	41	37	41	39
Or	30	24	31	30	29	32	27	35	29	28	28	28	27	28	27	20	29	36	30	27
Ab	35	38	36	38	37	34	34	31	35	36	36	37	36	35	32	36	31	27	29	34
sill					X		X	X					X						X	X
cord							X	X	X				X						X	X
TZrn °C							742	734	734	741	739	736	739	746	708	647	690	670	760	744
TREE °C							781	767	781	781	__	__	782	798	738	683	701	681	790	797